HIGH PERFORMANCE SHORT WAVELENGTH INFRARED FOCAL PLANE ARRAYS

A THESIS SUBMITTED TO
THE GRADUATE SCHOOL OF NATURAL AND APPLIED SCIENCES
OF
MIDDLE EAST TECHNICAL UNIVERSITY

BY

KÜBRA ÇIRÇIR

IN PARTIAL FULFILLMENT OF THE REQUIREMENTS
FOR
THE DEGREE OF MASTER OF SCIENCE
IN
ELECTRICAL AND ELECTRONICS ENGINEERING

FEBRUARY 2017

Approval of the thesis:

HIGH PERFORMANCE SHORT WAVELENGTH INFRARED FOCAL PLANE ARRAYS

submitted by **KÜBRA ÇIRÇIR** in partial fulfillment of the requirements for the degree of **Master of Science in Electrical and Electronics Engineering Department**, **Middle East Technical University** by,

Prof. Dr. Gülbin Dural Ünver _____
Dean, Graduate School of **Natural and Applied Sciences**

Prof. Dr. Tolga Çiloğlu _____
Head of Department, **Electrical and Electronics Eng.**

Prof. Dr. Cengiz Beşikci _____
Supervisor, **Electrical and Electronics Eng. Dept., METU**

Examining Committee Members

Prof. Dr. Haluk Külah _____
Electrical and Electronics Eng. Dept., METU

Prof. Dr. Cengiz Beşikci _____
Electrical and Electronics Eng. Dept., METU

Assoc. Prof. Dr. Barış Bayram _____
Electrical and Electronics Eng. Dept., METU

Prof. Dr. Mehmet Parlak _____
Physics Dept., METU

Assoc. Prof. Dr. Bülent Aslan _____
Physics Dept., Anadolu Uni.

Date: 03.02.2017

I hereby declare that all information in this document has been obtained and presented in accordance with academic rules and ethical conduct. I also declare that, as required by these rules and conduct, I have fully cited and referenced all material and results that are not original to this work.

Name, Surname: Kübra Çırçır

Signature:

ABSTRACT

HIGH PERFORMANCE SHORT WAVELENGTH INFRARED FOCAL PLANE ARRAYS

Çırçır, Kübra

M.S., Department of Electrical and Electronics Engineering

Supervisor: Prof. Dr. Cengiz Beşikci

February 2017, 82 pages

Short Wavelength Infrared (SWIR) band is desirable for many applications such as night vision, spectroscopy and hyperspectral imaging. Indium Gallium Arsenide ($In_{0.53}Ga_{0.47}As$) is a suitable material for SWIR photodetectors. This thesis focuses on the investigation of the pixel characteristics of a 15 μm pitch large format (640x512) focal plane array (FPA) with $In_{0.53}Ga_{0.47}As$ absorber and $Al_{0.52}In_{0.48}As$ p-type cap layers as an alternative to the conventional $In_{0.53}Ga_{0.47}As$ detectors utilizing InP as the p-cap layer. The FPA pixels were fabricated in the mesa structure in order to provide a comparison to the conventional planar type pixel arrangement. The dark current density of the FPA pixels was measured as 96 $\mu A/cm^2$ at 290 K. In order to determine the dominant dark current component, a model including diffusion, generation-recombination (G-R) and shunt currents is adopted. The results of fitting indicate that large area ($\geq$ 75x75 μm^2) pixels display bulk G-R dominated dark current behavior with the dark current density independent of the pixel dimensions. The trap characteristics extracted from fitting of G-R lifetime curve display an activation energy of 0.17 eV with respect to the intrinsic level (E_i), which is in

reasonable agreement with the Deep Level Transient Spectroscopy (DLTS) characterization results. On the other hand, as pixel-pitch decreases to 15 μm, surface related G-R component becomes the dominant dark current component. Therefore, the above mentioned trap density should be decreased and the passivation of the mesa sidewalls should be improved in order to improve the mesa-type FPA pixel performance.

Keywords: InGaAs, Short Wavelength Infrared, Focal Plane Array, Photodetector, DLTS, Deep Level Traps.

ÖZ

YÜKSEK PERFORMANSLI KISA DALGABOYU KIZILÖTESİ ODAK DÜZLEM DİZİNLERİ

Çırçır, Kübra

Yüksek Lisans, Elektrik ve Elektronik Mühendisliği Bölümü

Tez Yöneticisi: Prof. Dr. Cengiz Beşikci

Şubat 2017, 82 sayfa

Kısa Dalga Boyu Kızılötesi (SWIR) bandı gece görüşü, spektroskopi, hiperspektral görüntüleme gibi birçok uygulama için önemlidir. Indiyum galyum arsenit ($In_xGa_{1-x}As$) SWIR fotodedektörler için uygun bir malzemedir. Bu tez çalışması, p şapka katmanı olarak InP kullanan geleneksel $In_{0.53}Ga_{0.47}As$ dedektörlere alternatif olarak $In_{0.53}Ga_{0.47}As$ emici katmanı ve $Al_{0.52}In_{0.48}As$ p şapka katmanına sahip 15 µm pixel adımlı geniş formatlı (640x512) odak düzlem dizini (ODD) piksellerinin karakteristiklerinin araştırılmasına odaklanmıştır. ODD pikselleri geleneksel planar tipi piksellerle karşılaştırma olanağı sağlamak için mesa yapısında üretilmiştir. ODD piksellerinin karanlık akım yoğunluğu 290 K sıcaklıkta 96 $\mu A/cm^2$ olarak ölçülmüştür. Baskın karanlık akım bileşenini belirlemek için difüzyon, jenerasyon-rekombinasyon (J-R) ve şant akımlarını içeren bir model benimsenmiştir. Karanlık akım modellemesi sonuçları geniş alanlı ($\geq$ 75x75 μm^2) piksellerin piksel

boyutundan bağımsız karanlık akım yoğunluğuna sahip olduğunu ve karanlık akımda hacimsel J-R akımın baskın olduğunu sergilemektedir. Karanlık akımın J-R bileşeninden elde edilen tuzak seviyesi intrinsik seviyeden (E_i) 0.17 eV uzakta olan bir aktivasyon enerjisi vermekte olup, bu sonuç Derin Seviye Tranzient Spektroskopi (DLTS) karakterizasyon sonuçları ile uyumludur. Bununla birlikte, piksel adımı 15 µm'ye düşürüldüğünde yüzey ilişkili J-R bileşeni baskın karanlık akım birleşeni olmaktadır. Dolayısıyla, ODD piksel performansını artırmak için yukarıda bahsedilen tuzak yoğunluğunun azaltılması ve mesa yüzeyi pasivasyonunun iyileştirilmesi gereklidir.

Keywords: InGaAs, Kısa Dalgaboyu Kızılötesi, Odak Düzlem Dizini, Fotodedektör, DLTS, Derin Seviye Tuzakları.

To my mother

ACKNOWLEDGMENTS

I would like to express my sincere thanks to my supervisor Prof. Dr. Cengiz Beşikçi for his excellent guidance, supervision and providing me the possibility to work in such a sophisticated laboratory.

I would like to thank Prof. Dr. Haluk Külah, Prof. Dr. Mehmet Parlak, Assoc. Prof. Dr. Barış Bayram and Assoc. Prof. Dr. Bülent Aslan for being in my thesis committee.

I would like to thank Assist. Prof. Dr. Serdar Kocaman for his support, advices and for allocating the necessary resources.

I would like to thank Optonik Ltd. for facilitating optical characterization and Mikro-Tasarim Ltd. for supplying ROICs.

I would like to thank M. Halit Dolaş for his support, invaluable friendship and for sharing with me his knowledge about fabrication process.

I would like to thank Nardin Avishan for her help about using of DLTS setup and her friendship.

I would like to thank Fatih Uzgur, Muammer Kozan, Utku Karaca, Ekin Kızılkan, Göktuğ Özmen and Ekin Karaca for their friendship.

I would like to thank Mr. Özgür Şen for his extra effort to keep the laboratory running and his friendship.

It is not possible to complete my acknowledgement without expressing my gratitude to my friends. I would like to thank Burak Duran for his encouragement and consistent help. I am also grateful to Emre Alp Miran, Ramazan Çetin and Havva Erdinç for their emotional support and patience.

Last but not least, I would like to present my sincere appreciation to my sister Assist. Prof. Dr. Esra Öztürk and my family.

TABLE OF CONTENTS

LIST OF FIGURES

FIGURES

CHAPTER 1

INTRODUCTION

The existence of infrared (IR) radiation was first discovered by Sir William Herschel two centuries ago. He proved experimentally that the spectrum of light contains some form of invisible rays by using a thermometer and a simple prism to separate sunlight into its spectral components. Since his pioneering work, IR radiation has been the basis of several technologies including spectroscopy, hyperspectral imaging and night vision. According to application needs, many different physical mechanisms and material systems can be utilized in order to detect IR radiation.

In the detection of Short Wavelength Infrared Radiation (SWIR), the most commonly used material systems are Germanium (Ge), Mercury Cadmium Telluride (HgCdTe) and Indium Gallium Arsenide (InGaAs). In this thesis work, $In_{0.53}Ga_{0.47}As$ grown lattice-matched on InP substrate with molecular beam epitaxy (MBE) was utilized for the fabrication of SWIR detectors. The detectors were fabricated in the mesa structure in order to provide data for comparison with conventional planar structure. In the SWIR band, lower dark current and smaller pixel pitch are desirable for imaging at night due to small amount of photon flux in this band interval. This thesis work focuses on the fabrication of 15 μm focal plane arrays (FPAs) and the determination of performance limiting factors as the pixel pitch decreases. With the purpose of identifying the performance limiting factor and providing a feedback to the following works, dark current modeling is conducted and the results are linked to those of deep level transient spectroscopy (DLTS) measurements.

This chapter presents the basics of IR radiation, infrared detector types and the most significant performance parameters of photon detectors.

Chapter 2 presents the application area of SWIR photon detectors in detail. This chapter also includes a literature survey on large format (640x512) $In_{0.53}Ga_{0.47}As$ lattice matched to InP substrate focal plane arrays (FPAs) with 15 μm pixel pitch.

Chapter 3 presents the fabrication of InGaAs SWIR FPAs, I-V characterization of large area (≥ 75x75 μm^2) pixels and FPA pixels. In order to investigate the origin of dark current for both large area pixels and FPA pixels, a model including diffusion current, generation-recombination (G-R) current, and shunt current is adopted. The properties of trap extracted from dark current modeling are also investigated by using Deep Level Transient Spectroscopy (DLTS) method.

Finally, Chapter 4 presents the conclusion of this thesis work.

1.1. Basics of Infrared Radiation

Infrared (IR) radiation is a form of electromagnetic wave whose band is a small portion of entire electromagnetic spectrum lying between 700 nm and 100 μm. The classification of IR bands related to detector technology is as follows [1]

- Near infrared (NIR): 700-1000 nm
- Short wavelength infrared (SWIR): 1-3 μm
- Medium wavelength infrared (MWIR): 3-5 μm
- Long wavelength infrared (LWIR): 5-14 μm
- Very long wavelength infrared (VLWIR): 14-30 μm
- Far infrared (FIR): 30-100 μm.

Objects with temperature above absolute zero (0 K) emit electromagnetic radiation due to vibrational motion of atoms. The amount of radiation energy emitted at a particular wavelength is directly related to the temperature and the emissivity of a material. Objects also absorb electromagnetic radiation depending on the interaction of materials with the incident radiation. Actually, the interaction between material and incident radiation results in three ways: reflectance, absorbance and transmittance given by Equation 1.1, 1.2 and 1.3, respectively. According to Kirchhoff's Law of Thermal Radiation, the sum of these parameters is equal to unity

as given in Equation 1.4. Before Kirchhoff's Law was recognized, it had been experimentally established that a good absorber was a good emitter (α=ε) [2].

$$\rho(\text{reflectance}) = \frac{energy\ reflected}{incident\ energy} \tag{1.1}$$

$$\alpha(\text{absorbance}) = \frac{energy\ absorbed}{incident\ energy} \tag{1.2}$$

$$T(transmittance) = \frac{energy\ transmitted}{incdent\ energy} \tag{1.3}$$

$$\rho + \alpha + T = 1 \tag{1.4}$$

Being an ideal radiation absorber and also ideal radiation emitter, the blackbody is of primary importance in studying thermal radiation and the fundamental laws of radiation. Blackbody emits the highest radiation power theoretically at any temperature in all wavelengths, and consequently, it is utilized as a standard for comparison with the radiation of real physical bodies. For a given material, emissivity can be evaluated as the ratio of the total exitance radiated by a material at temperature T to the total exitance of a blackbody at the same temperature. It is clearly evident from Equation 1.5 that emissivity of a blackbody is equal to unity [3].

$$\varepsilon(\text{emissivity}) = \frac{M_{actual}}{M_{ideal\ blackbody}} \tag{1.5}$$

Spectral exitance can be defined as the radiation power emitted from a surface per unit area per unit wavelength at a given temperature. The spectral exitance of a blackbody is described by Planck's Law expressed as [4]

$$M_\lambda(\lambda, \mathrm{T}) = \frac{2\pi hc^2}{\lambda^5(e^{\frac{hc}{\lambda kT}} - 1)} \tag{1.6}$$

where $M_\lambda(\lambda, \mathrm{T})$ is the spectral radiant exitance in Watt/cm^{2}μm, h is the Planck's constant, c is the speed of light, λ is the wavelength, k is the Boltzmann constant, and

T is the blackbody temperature. Figure 1.1 shows a series of blackbody spectral exitance at different temperatures.

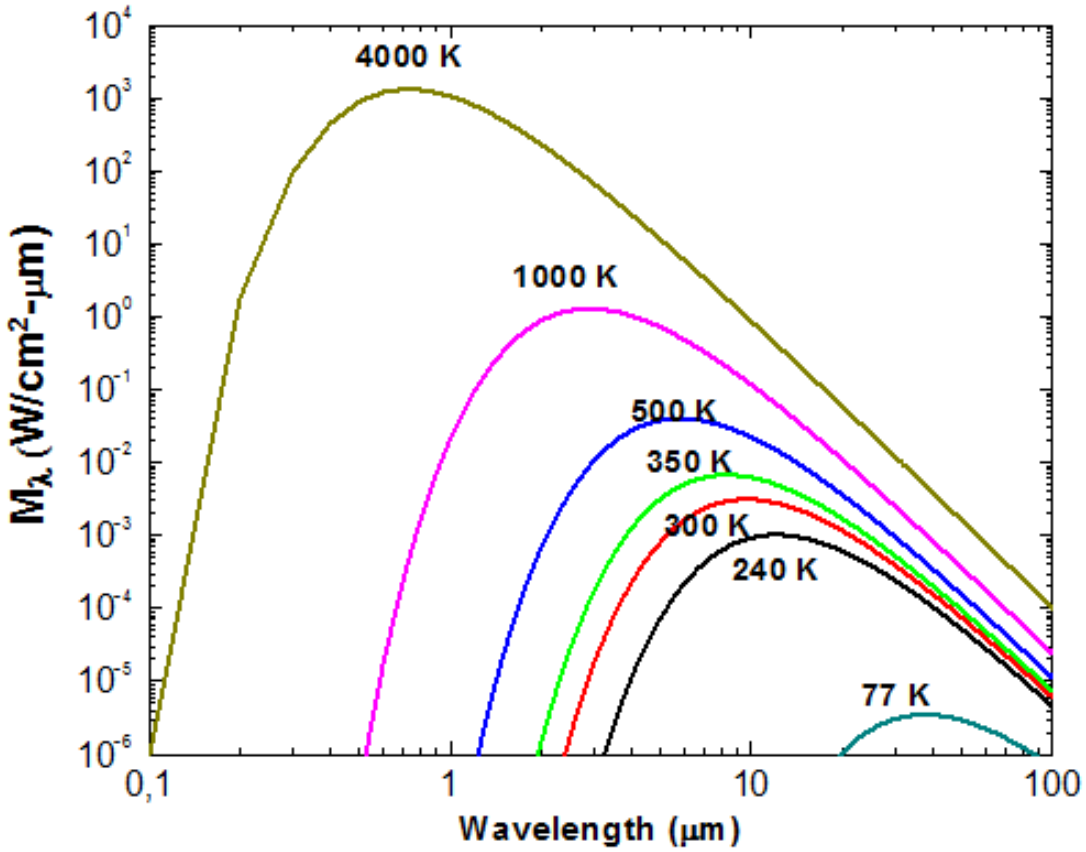

Figure 1.1: Blackbody spectral exitance at different temperatures [5].

As it can be seen from Figure 1.1, the peak emittance occurs at a smaller wavelength as the temperature increases, which is known as the Wien's displacement law expressed as

$$\lambda_{max} = \frac{2898\ \mu m.K}{T(K)} \tag{1.7}$$

where λ_{max} is the wavelength of maximum emittance in μm and T is the temperature of the object in K. The area under the entire curve for a specific temperature can be calculated by integrating the Planck's equation between $\lambda = 0$ and $\lambda = \infty$. The total blackbody exitance can be found as follows [6]

$$M_\lambda(\text{total}) = \sigma T^4 \ (W/cm^2) \tag{1.8}$$

where σ is the Stefan-Boltzmann's constant which has a value of 5.67×10^{-12} W·cm^2·K^{-4}.

Basically, the detection of self-emission of an object is defined as thermal imaging. Thermal imaging can be applicable in MWIR, LWIR and VLWIR band of IR spectrum. For the objects at 300 K, the wavelength of maximum emittance is around 10 μm, which lies in the LWIR band. However, MWIR detectors are preferred generally for thermal imaging at room temperature to achieve more compact system. The reason for that is MWIR band is less affected by diffraction facilitating smaller pixel pitch. Furthermore, due to the larger bandgap, a detector operating in the MWIR band has lower dark current, which means that cooling requirement is less. It is seen from Figure 1.1 that the amount of photon flux in the LWIR band is higher than that in the MWIR band for near room temperature objects. Even though LWIR region has higher exitance, MWIR region provides higher thermal contrast.

There is another band interval where infrared imaging can be done. As it can be clearly seen from Figure 1.1, thermal imaging of room temperature objects is practically impossible in SWIR region due to the lack of sufficient photon flux. However, reflected light is utilized for imaging in SWIR detectors in contrast to MWIR and LWIR detectors. In this case, light source which can be natural or artificial is required. SWIR images resemble visible images as SWIR cameras make use of reflected lights.

In order to detect IR radiation emitted by an object, it is essential to investigate its propagation through the atmosphere. The percentage of radiation transmitted at various wavelengths through the atmosphere is given in Figure 1.2.

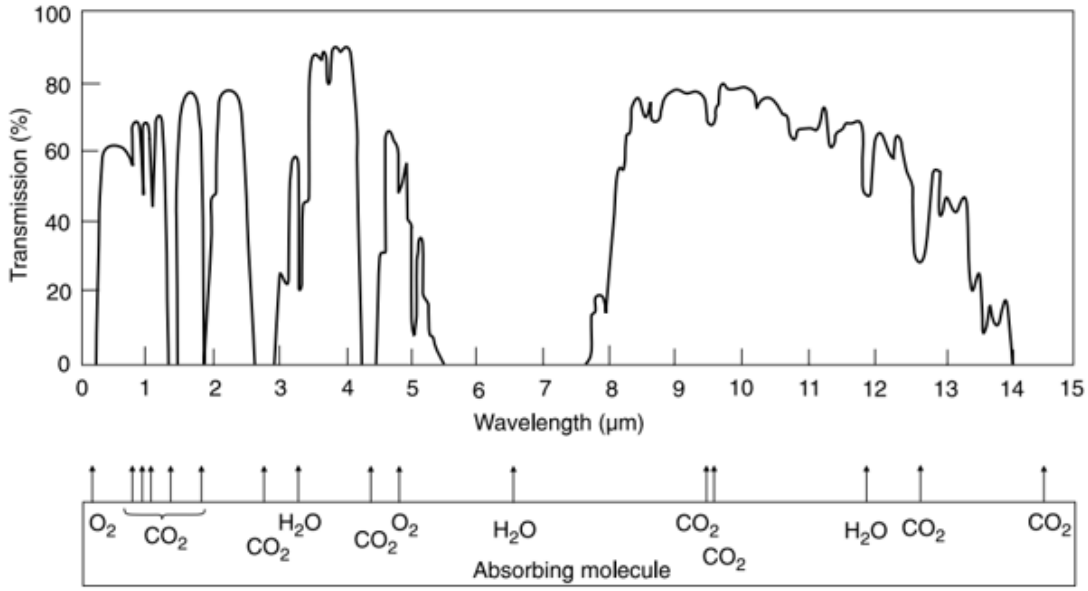

Figure 1.2: Atmospheric transmission and the absorbing molecules at sea level and through 1800 m horizontal path [7].

When IR radiation travels through the atmosphere, it is attenuated exponentially due to scattering by particles and absorption by the atmospheric gasses. Scattering results from interaction of photons with atmospheric molecules such as CO_2, ozone and nitrogen. In addition, scattering is also caused by atmospheric aerosols such as fog, smog and dust. Scattering is wavelength independent if the particle size is much larger than the wavelength of the radiation. However, as the size of the particle gets closer to the wavelength of radiation, scattering rate becomes strongly wavelength dependent.

Another mechanism responsible for the attenuation of radiation is absorption. Gas molecules leading to absorption are water vapor (H_2O), carbon dioxide (CO_2) and ozone (O_3). The concentration of water vapor may change with space and time. For horizontal paths, H_2O and CO_2 play an important role in absorption.

As clearly seen from Figure 1.2, there is a plenty of atmospheric transmission in SWIR, MWIR and LWIR region. These regions are called atmospheric windows. On the other hand, there is a great deal of atmospheric absorption between MWIR and

LWIR band. Both passive and active sensing technologies do best if they operate within the atmospheric windows.

1.2. Types of Infrared Detectors

An IR detector is a device converting radiation energy into measurable physical quantity. For this purpose, many different physical mechanisms can be used. Based on the origin of detection principle, IR detectors are classified into two broad categories: thermal detectors, photon detectors.

1.2.1. Thermal Detectors

Thermal detectors absorb incident IR radiation, and this radiation gives rise to a change in temperature which in turn gives rise to a change in some material properties such as conductivity, resistance and dielectric properties. These changes are observed as an electrical signal at the output.

Thermal detectors are mainly divided into three groups according to their detection mechanisms. These are thermoelectric detectors (thermopiles), pyroelectric detectors, and microbolometers.

Thermoelectric (Thermopiles) Detectors: A thermocouple is composed of two different materials, which are brought into contact at one end and the other two ends are attached to a voltage meter. When common junction is subjected to radiation, a so-called thermovoltage is observed at other end due to thermoelectric effect. In order to make the system more sensitive, multiple thermocouples are connected in series. The resulting system is called thermopile.

Pyroelectric Detectors: It is possible to change the polarization of any material with electric field depending on its permittivity and dielectric constant. However, pyroelectric detectors become spontaneously polarized even when there is no electric field. The reason of this polarization is temperature fluctuations. The response of this type of material to changes in the temperature is observed as a potential difference between the opposite faces.

Microbolometers: Resistor-based microbolometers have an absorber layer that absorbs incident radiation and converts it into heat. This thermal energy causes a change in the resistance of detector material. This change in such an electrical property can be read with a suitable circuitry. In order to provide thermal isolation, the temperature sensitive part is suspended from the structure it is constructed on.

1.2.2. Photon Detectors

In this type of detectors, operation principle is based on the interaction of incident photons with electrons. When photons come into interaction with a semiconductor, electron hole pairs (EHPs) are created if their energy is greater than fundamental bandgap of this material. Energy of photons can be expressed as

$$E_g\,(eV) = \frac{1.24}{\lambda} \tag{1.9}$$

where λ is the wavelength of the incident radiation in μm.

As it is evident from Equation 1.9, photon detectors display wavelength dependent behavior in contrast to thermal detectors. Cut-off wavelength of photon detectors is reached when incident photon energy is equal to energy bandgap of the semiconductor.

After the absorption of photons, free charge carriers are collected at the output contacts with the help of an electric field. According to generation of this electric field, which can be applied externally or built internally, photon detectors are divided into two main groups: photoconductive and photovoltaic.

Photoconductive (PC) Detectors: In photoconductive (PC) detectors, photon absorption creates EHPs. These photo-generated free charge carriers increase the conductivity of semiconductor. In order to prevent recombination of the photo-generated carriers before they reach the contacts, sufficiently large external bias voltage should be applied. Thanks to external bias voltage, photo-generated charge carriers contribute to the current, called as photocurrent (I_{photo}). The amount of photocurrent is directly proportional to the photon flux (ϕ). The illustration of a

photoconductor detector and charge carrier generation process are shown in Figure 1.3.

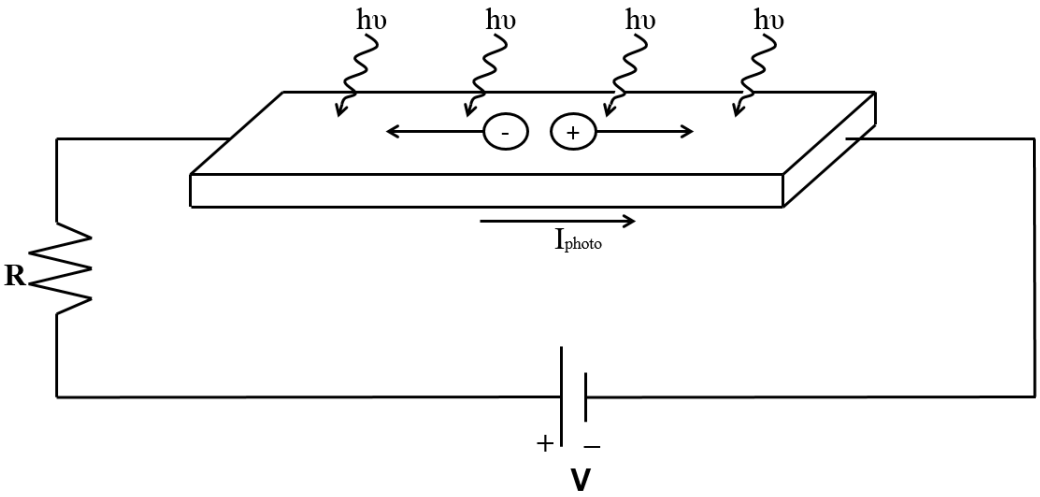

Figure 1.3: The illustration of a single photoconductor and generation of EHPs inside semiconductor material.

In order to achieve high responsivity in photoconductive detectors, a bias voltage large enough should be applied, which in turn results in higher power dissipation. For that reason, photoconductive detectors are not suitable for large format focal plane arrays (FPAs).

Photovoltaic (PV) Detectors: In photovoltaic (PV) detectors, the formation of EHPs is similar to that of PC detectors. One of the most widely used PV detectors is p-n junction semiconductor, which is often referred as a photodiode. The operation of p-n photodiode is shown in Figure 1.4. Instead of using external bias, PV detectors make use of built-in electric field to sweep out photo-generated charge carriers across the depletion region. The origin of built-in electric field relies on uncompensated charge which results from the diffusion of electrons and holes due to concentration gradients. The photocurrent observed as the output signal of the detector can be expressed as

$$I_{photo} = q\eta A\phi \tag{1.10}$$

where q is the charge of electron, η is the quantum efficiency which is the number of EHPs crossing the junction per incident photon, A is the area of the photodiode, and ϕ is the incident photon flux.

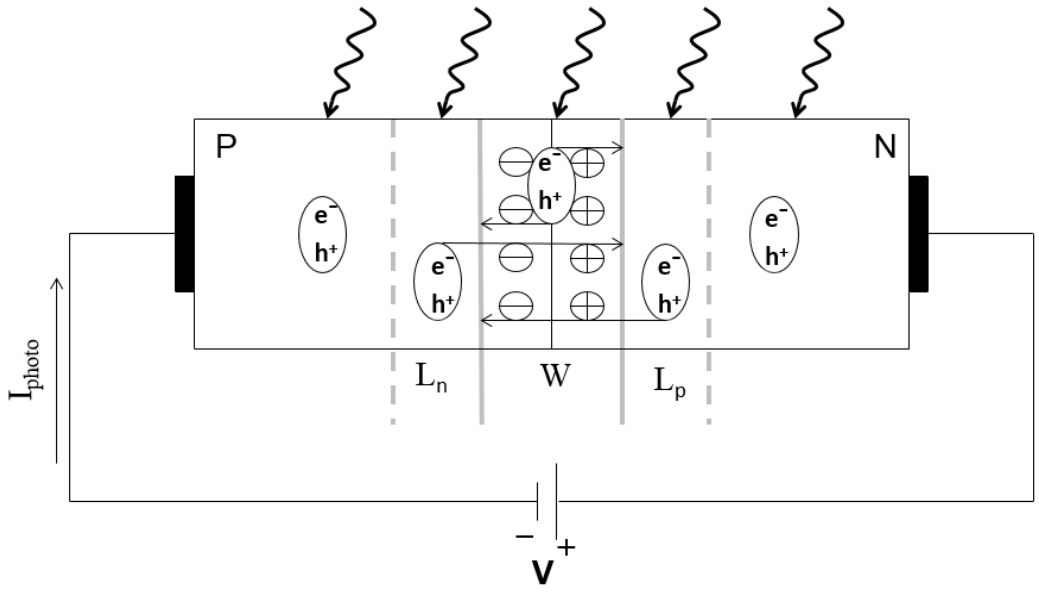

Figure 1.4: The illustration of PV detector and generation of EHPs.

Figure 1.5 shows the current-voltage characteristic of a p-n photodiode under illuminated and non-illuminated conditions. Under dark condition, EHPs are created thermally and this current is referred as dark current, I_{dark}. Under illumination, photo-generated current, I_{photo} is added to dark current.

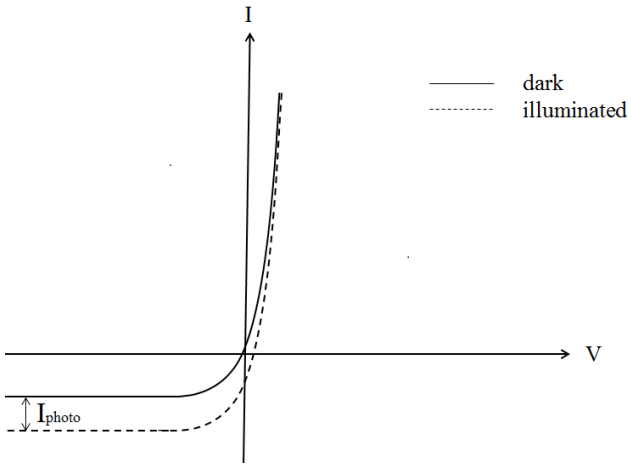

Figure 1.5: Schematic representation of current-voltage characteristic of a photodiode under dark and illuminated conditions.

From another point of view, photon detectors may also be classified depending on the nature of energy transition caused by interaction of photons with electrons. Figure 1.6 depicts the interaction of photons with electrons bound to lattice atoms and to impurity atoms or with free electrons.

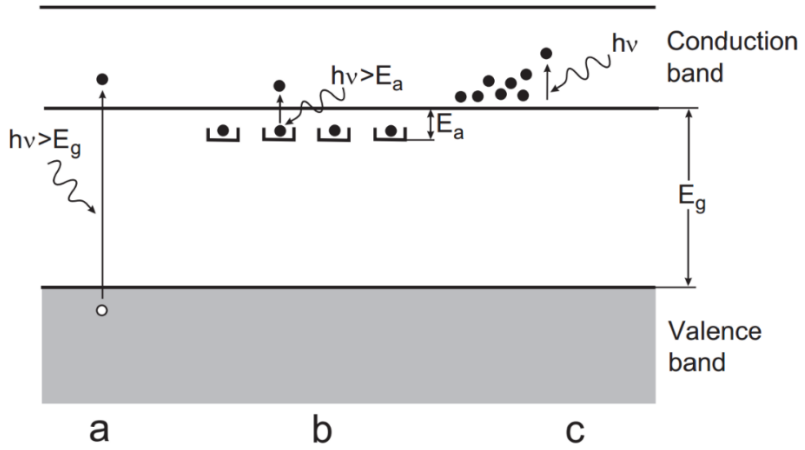

Figure 1.6: Optical energy transition in semiconductor: (a) intrinsic absorption, (b) extrinsic absorption, and (c) free carrier absorption [8].

According to transition mechanisms, the most important detector types are: intrinsic, extrinsic, quantum well and superlattice detectors.

Intrinsic Photon Detectors: In the class of intrinsic photon detectors, electrons are excited from valence band to conduction band in the semiconductor material. It is possible to excite electrons in two ways: by thermal energy and by photons. The resultant components of total current observed at the output compete with each other. While lower bandgap materials require cryogenic cooling in order to suppress thermally generated current component, larger bandgap materials utilized in the detection of smaller wavelengths provide an opportunity of operating at room temperature [9]. As commonly known, cryogenic cooling requirement makes the system more bulky, heavy and expensive.

In intrinsic photon detectors, the minimum energy required for absorption is the energy bandgap of semiconductor. Therefore the cut-off wavelength of intrinsic photon detectors is determined by the energy bandgap of semiconductor materials.

The most commonly used intrinsic detector materials are HgCdTe, InGaAs, InAs, InSb, and InAsSb which will be discussed in more detail in Chapter 2.

Extrinsic Photon Detectors: In the class of extrinsic photon detectors, an impurity level close to the conduction band is introduced by doping. The excitation of electrons takes place between the impurity level and the conduction band. The energy difference between impurity level and conduction band determines the cut-off wavelength of this type of detectors. The main disadvantage of extrinsic photon detectors is the requirement for much more cooling power in comparison with intrinsic photon detectors. Therefore, intrinsic photon detectors are generally preferred for the detection of shorter wavelengths below 20 μm [8].

Quantum Well Infrared Detectors (QWIPs): QWIP is one of the simplest quantum mechanical structures, which utilizes intersubband transition for the detection of IR radiation. By combining a smaller bandgap material with a larger bandgap material, 1-D electron confinement is created as illustrated in Figure 1.7.

Besides multi-color capabilities, QWIPs are grown in higher quality level by making use of mature III-V material technology. Due to higher material quality, large format FPAs can be fabricated as an alternative to narrow bandgap detectors operating at lower temperatures (< 70 K) [9].

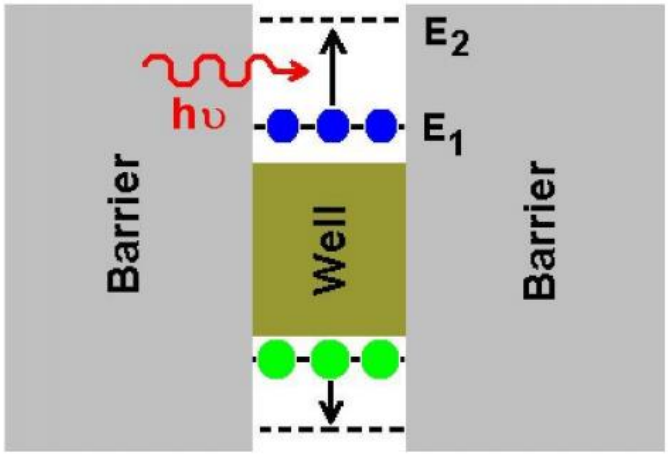

Figure 1.7: The illustration of energy bandgap diagram and quantized energy states of QWIP [10].

Superlattice Structure: In superlattice structure, the bandgap of two different materials is misaligned with each other periodically in order to form an artificial bandgap. Figure 1.8 illustrates InAs/GaInSbAs Type II strained layer supperlattice (SLS). As a result of overlapping wavefunction of electrons in the conduction band of InAs and overlapping wavefunction of holes in the valence band of GaInSb, electron and hole minibands are created, which may be called a virtual bandgap.

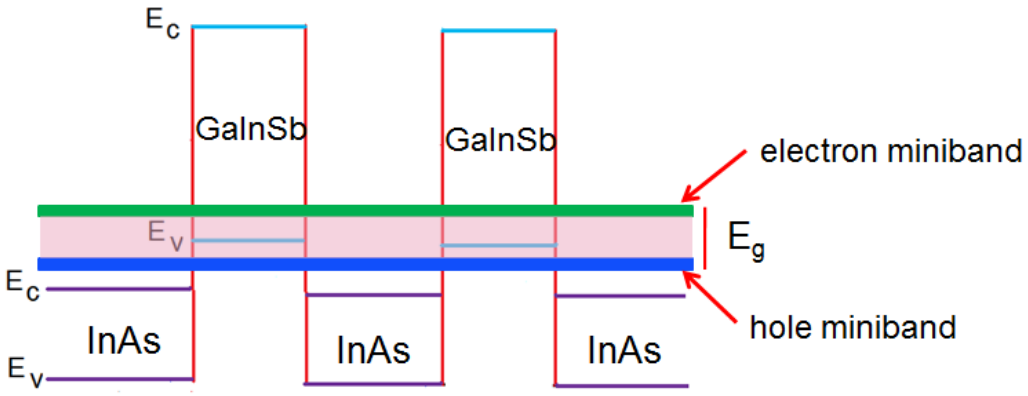

Figure 1.8: The illustration of energy bandgap of Type–II supperlattice structure and the formation of artificial bandgap [5].

1.3. Figure of Merits

To be able to evaluate or compare IR photon detectors in terms of performance, some measurable parameters are required. In this section, the most important performance parameters are introduced. These parameters can be listed as follows

1. Responsivity
2. Noise
3. Detectivity

1.3.1. Responsivity

Responsivity is a parameter showing how much electrical output signal produced in response to incoming IR radiation. The responsivity of photon detectors can be expressed as follows

$$Responsivity(R) = \frac{Output\ Signal\ (A\ or\ V)}{\phi} = \frac{I_{photo}\ (A)}{\phi} \tag{1.11}$$

where ϕ is total radiation power falling on the detector. As illustrated in Figure 1.9, responsivity exhibits different characteristics based on the unit definition. It is possible to express output signal in volt or ampere and incoming radiation in photons per second or Watts. The most commonly used unit for responsivity is ampere per Watts.

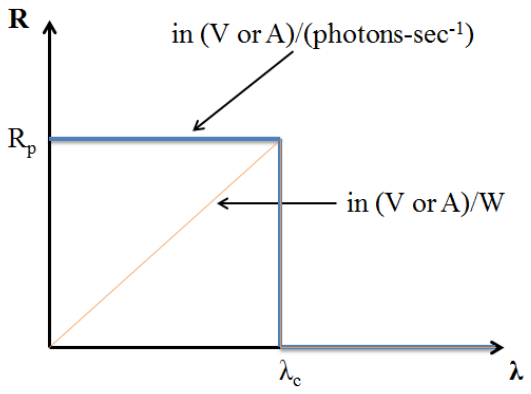

Figure 1.9: The illustration of responsivity versus wavelength in terms of two different units.

When ϕ is specified in terms of photons per second, responsivity displays a wavelength independent behavior. The wavelength independent behavior of responsivity results from the fact that output signal i.e, photocurrent is directly proportional to the number of photons. If ϕ is defined in terms of Watts, responsivity displays a behavior depending on the wavelength. The wavelength dependency of responsivity is called spectral responsivity expressed as

$$R = q\eta g\frac{\lambda}{hc} \tag{1.12}$$

where q is the charge of electron, η is the absorption quantum efficiency, g is the photoconductive gain (which is the ratio of the number of electrons collected at the external circuit to the number of absorbed photons), λ is the detection wavelength, h

is the Planck's constant, and c is the velocity of light. While g is approximately equal to one for photovoltaic detectors in most of the cases [11], photoconductive detector gain (g) changes with the ratio of electron recombination lifetime to the transit time assuming that electron mobility is much larger than hole mobility.

1.3.2. Noise

Although photon detectors have desired responsivity, they may suffer from noise. Therefore, noise level of the system should be taken into consideration in order to predict performance of detectors. Noise is defined as the rms deviation of signal from its average value. There are several noise mechanisms for photon detectors such as Johnson noise, generation-recombination (g-r) noise, shot noise, and 1/f noise.

Johnson (Nyquist or Thermal) Noise: Thermal noise was first realized by Sir Johnson. Then it was explained theoretically by Sir Nyquist in 1928. This noise originally results from thermally generated charge carriers causing fluctuation at the signal output. Even when no bias is applied, thermal noise can be observed in a conductor at the temperatures above 0 K. Thermal noise is a WHITE noise meaning that the amplitude of this noise is independent of the frequency. It can be formulated mathematically as follows

$$i_{n_{Johnson}} = \sqrt{\frac{4kT\Delta f}{R}} \tag{1.13}$$

where k is Boltzmann's constant, R is the resistance and Δf is the bandwidth.

Generation Recombination (GR) Noise: GR noise is due to fluctuations in the number of charge carriers generated optically and thermally. The noise associated with optical generation arises from the random arrival of photons. GR noise is expressed as

$$i_{n_{gr}} = \sqrt{4qI_{total}g\Delta f} \tag{1.14}$$

where q is the charge of electron, g is the gain of the photoconductor and Δf is the bandwidth. The total current I_{total}, is the sum of dark current, I_{dark} and photocurrent, $I_{photo.}$ Dark current can be suppressed by lowering the detector temperature which results in photocurrent being much greater than dark current. When photocurrent becomes the dominant current component, background limited performance (BLIP) condition is achieved.

Shot (Photon) Noise: In contrast to Johnson noise, an external bias must be applied to observe shot noise. Shot noise of a detector is expressed as [2]

$$i_{n_{gr}} = \sqrt{2qI\Delta f}\ (A) \tag{1.15}$$

where q is the charge of electron, I is the device current and Δf is the bandwidth.

1/f (Pink) Noise: Although the main reason of 1/f noise is not evident yet, it is a well-known fact that the spectral density of 1/f noise is inversely proportional to frequency over a wide range [2].

1.3.3. Noise Equivalent Power and Detectivity

Detectivity is an important performance parameter for assessment or comparison of different detectors. Responsivity shows only how much signal is observed in response to radiation power falling on the detector. Therefore, a parameter called noise equivalent power (NEP) is defined to provide necessary information about noise level of detector. NEP can be defined as the radiation flux to achieve a signal output equivalent to noise signal. NEP is expressed as

$$NEP = \frac{\upsilon_{noise}}{R_v} = \frac{i_{noise}}{R_i} \tag{1.16}$$

where R_i is the current responsivity, R_v is the voltage responsivity, i_{noise} is the noise current, and υ_{noise} is the noise voltage. NEP should be small to lower the amount of minimum detectable radiation power.

In order to eliminate the dependency of NEP on detector area and measurement bandwidth, normalization is conducted. The result is described as specific detectivity (D*) given as

$$D^* = \frac{\sqrt{A_D\ \Delta f}}{NEP} = \frac{\sqrt{A_D\ \Delta f}}{v_{noise}} R_v = \frac{\sqrt{A_D\ \Delta f}}{i_{noise}} R_i \tag{1.17}$$

where A_D is the area of detector.

CHAPTER 2

SHORT WAVELENGTH INFRARED (SWIR) PHOTODETECTORS

In this section, Short Wavelength Infrared (SWIR) detectors are discussed in more detail. First, the application areas combined with remarkable features are covered and then various material systems with their advantages and disadvantageous are presented. Next, the physical structure of the conventional SWIR detectors will be shown and finally the state of art results from the literature are illustrated.

2.1 Application of SWIR Photodetectors

SWIR band is desirable for imaging applications in terms of the features such as haze and fog penetration, atmospheric transmission, cloud and smoke penetration, target and background contrasts, and long range target identification [12].These features make this technology important for the military applications. Furthermore, SWIR band is utilized for various applications such as optical communication at 1.55 μm, spectroscopy, non-destructive testing and hyperspectral analysis for industry and space applications.

Regarding the application needs, it is possible to categorize SWIR band into two categories [13].

- Category 1: applications which need a cut-off wavelength of 1.6 - 1.7 μm,
- Category 2: applications which need a cut-off wavelength greater than 1.7 μm, typically 2.5 μm,

The cut-off wavelengths specified in category 1 and 2 fulfill the requirements of SWIR applications with potential material systems. The cut-off wavelength of 1.7 μm is satisfied with Germanium (Ge), InGaAs lattice matched to InP substrate and HgCdTe. The cut-off wavelength of 2.5 μm is specifically named as extended wavelength SWIR. In the detection of extended SWIR wavelength, the most commonly used material systems are Indium Gallium Arsenide (InGaAs) lattice mismatched to InP substrate and Mercury Cadmium Telluride (HgCdTe). The detailed discussion about these materials is presented in section 2.2.

SWIR band is demanding for many applications due to some unique properties. Basically, the applications served by SWIR detectors make use of three main properties [14].

- Reduced scattering effect of longer wavelength (compared to visible range)
- Spectral signatures originating from molecular vibrations
- Illumination from sources that are invisible to human eye (such as active or passive illumination) or, alternatively, from thermal emissions emitted by objects with temperatures above 150 degrees Celsius.

The first of the surveillance advantages of SWIR cameras is the ability to see farther through the challenging atmospheric conditions such as haze and fog. Shorter wavelengths (e.g. visible range compared to SWIR) strongly suffer from a phenomenon known as Rayleigh scattering [14]. As clearly illustrated in Figure 2.1, more clear images are acquired by a SWIR camera since SWIR band is less scattered by molecules in the atmosphere. Another advantage of SWIR cameras over visible imagers is the ability to obtain high contrast images as demonstrated in Figure 2.2.

Figure 2.1: Images recorded under hazy conditions by a visible camera (left) and a SWIR camera (right) [12].

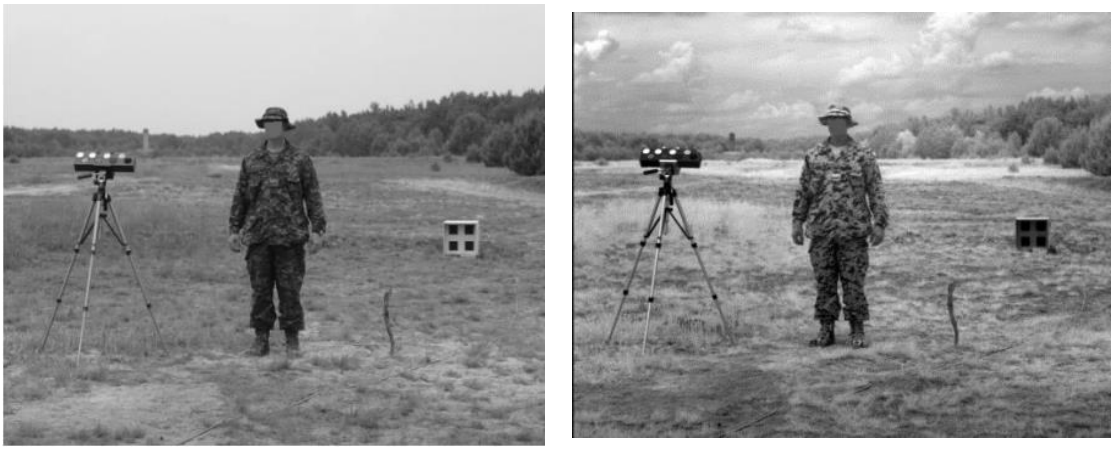

Figure 2.2: Battle dress uniform recorded by a visible camera (left) and a SWIR camera (right) [12].

Furthermore, another remarkable feature of SWIR cameras is the ability to see through the opaque materials such as plastic. Since SWIR imaging is based on the reflected light from an object, it is possible to recognize materials inside plastic bottles due to the difference among their spectral signatures. Spectral signature is defined as the difference in the reflectance characteristic of materials with respect to wavelength. As illustrated in Figure 2.3, the fill level of bottles is clearly evident.

Figure 2.3: The images of opaque and transparent bottles as recorded by a visible camera (left) and a SWIR camera (right) [15].

Hyperspectral imaging is also an application area of SWIR imaging. Hyperspectral remote imager records dozens or hundreds of images simultaneously in the narrow and adjacent wavelength bands. Then, a plot of brightness with respect to wavelength is obtained. In order to recognize surface material, its spectral signature is utilized for comparison with the measurement. Figure 2.4 shows the spectral signature of different materials.

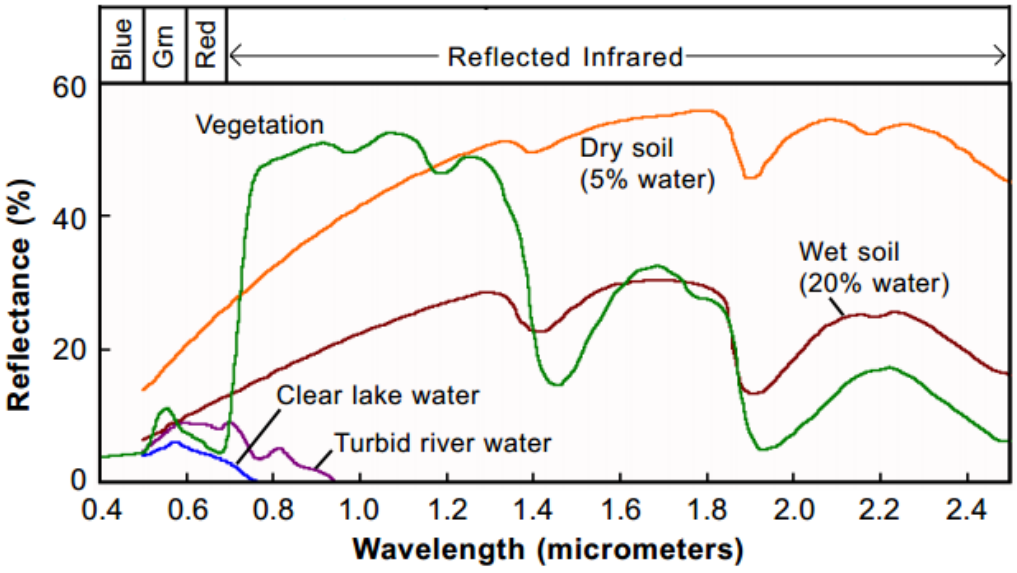

Figure 2.4: Measured spectral signatures of different materials [16].

As discussed in Chapter 1 in detail, SWIR imaging is based on the reflected radiation from the object rather than the self-emission which is the basis of thermal imaging. Thermal imaging is useful for detecting a warm body. However, it is not possible to determine the identity of a person accurately. While a thermal image of person is different from the visible image, an image recorded by a SWIR camera resembles an image recorded by a visible camera. In this case, it is much easier to identify people and features [17]. As illustrated in Figure 2.5, SWIR images have more detail when compared with the thermal image.

Figure 2.5: Images recorded by a thermal camera (left) [18] and a SWIR camera (right) [19].

Optical communication at 1.55 μm is another application area of SWIR band. As this specific wavelength provides the lowest loss for the fiber cable materials, SWIR products become important for long distance communication data links as well [20]. This wavelength is also desirable for the purpose of manufacturing eye-safe laser range finders in military applications. Furthermore, NIR/SWIR cameras are also capable of seeing 0.85 μm targeting lasers which have also a track in visible range. Figure 2.6 shows images of both laser designators.

Figure 2.6: Images of 0.85 and 1.55 μm laser designator spots marking a building on a moonless night [14].

Last but not the least, night vision is one of leading SWIR applications, where several detector technologies coexist. It is evident that SWIR detectors need some illumination sources due to the fact that their detection mechanism is based on the reflected light. These sources can be artificial, such as eye safe lasers or natural, such as sun, airglow, zodiacal light, star light and moonlight. These natural source emissions enable surveillance under passive illumination at night. Figure 2.7 shows irradiance levels for sources of night time illumination.

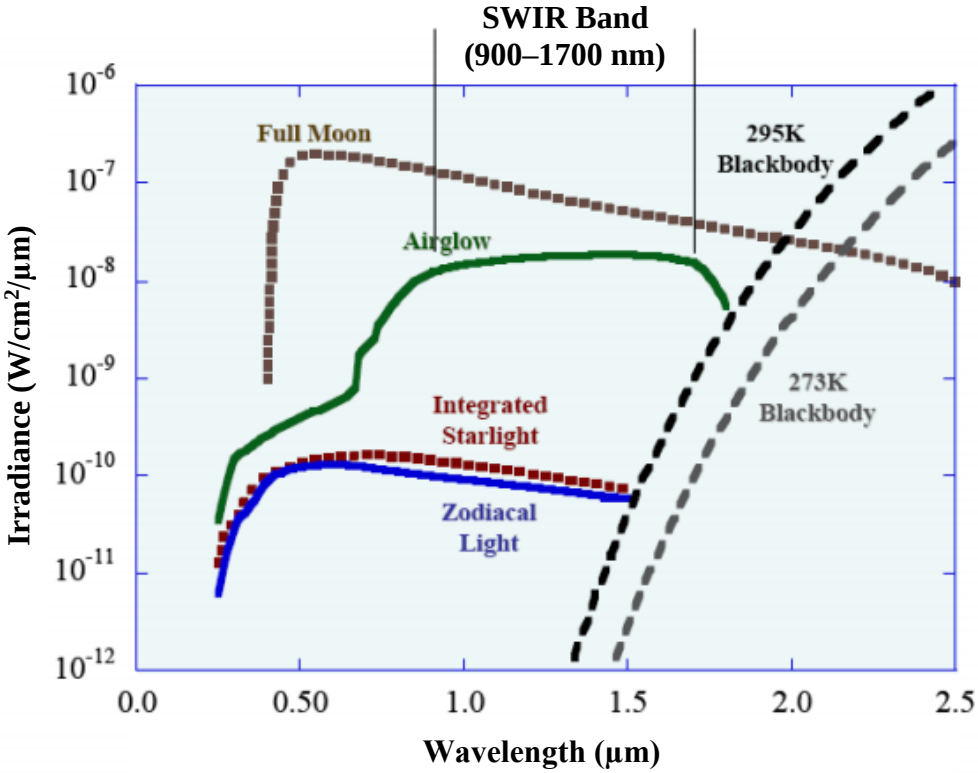

Figure 2.7: Different illumination sources for SWIR imaging at night [47].

As it can be clearly seen from Figure 2.7, the brightest source is the moon light at night. However, night vision in moonless nights is also possible due to airglow. Airglow is created by the relaxation of the hydroxyl molecules (OH) which are excited during the day in the upper atmosphere and radiate energy at various intensities throughout the night. Airglow irradiance is two orders of magnitude above starlight and overlaps with SWIR band. This can be a real advantage in dark night conditions such as moonless and cloudy skies [10,11]. Figure 2.8 illustrates the airglow radiation with and without moonlight.

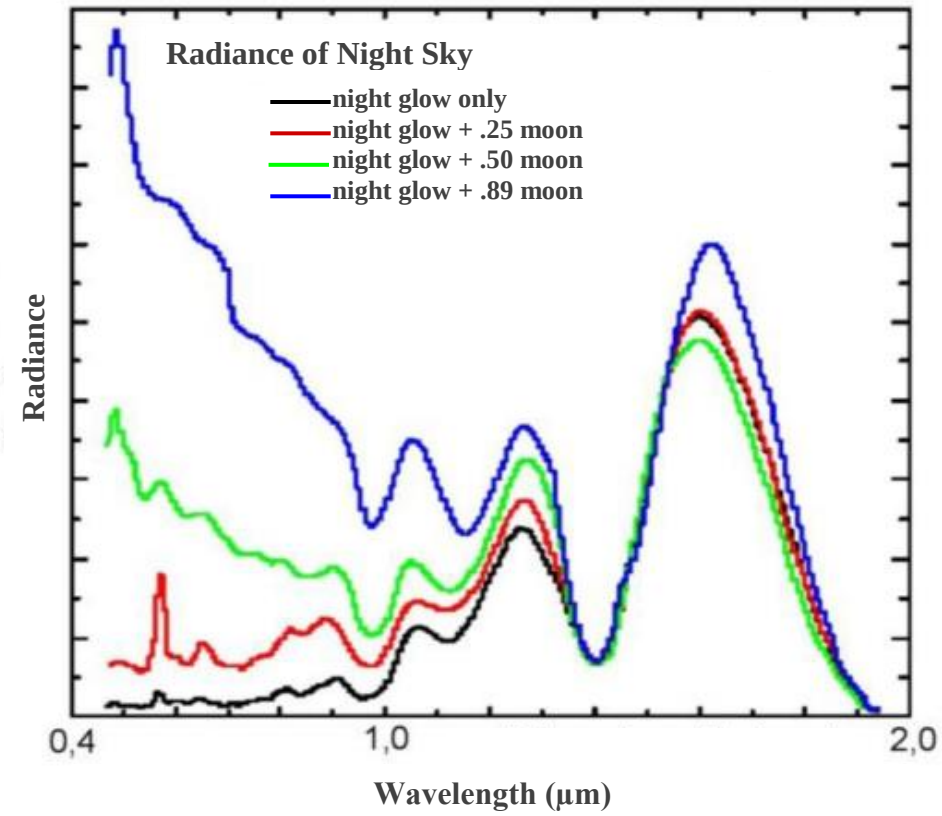

Figure 2.8: Spectral radiance of airglow with and without moonlight [24].

2.2 Material Systems for SWIR Photodetectors

In order to fulfill SWIR application requirements, a variety of photodetector materials can be utilized such as Germanium (Ge), Indium Gallium Arsenide (InGaAs) and Mercury Cadmium Telluride (MCT or HgCdTe). In this section, SWIR material systems are investigated in detail.

2.2.1 Germanium(Ge)

Germanium (Ge) grown on Silicon (Si) substrate offers low cost production for infrared detection from 0.4 µm to 1.6 µm. Ge-on-Si photodetectors benefit from the advantage of Si based technology and its compatibility with CMOS readout integrated circuit (ROICs). The compatibility of Ge-on-Si photodetectors with Si based ROICs is a promising feature in the sense of monolithic integration in which the same substrate is utilized for the fabrication of both photodetector and ROIC.

As commonly known, Ge is an indirect bandgap material. However, it has pseudo-direct bandgap behavior. With the introduction of band engineering, the transformation of Ge from indirect bandgap to direct bandgap can be realized. Figure 2.9 demonstrates L-valley, which corresponds to the indirect bandgap, and Γ-valley, which corresponds to the direct bandgap. The difference between L-valley and Γ-valley is only 136 meV. This difference can be further reduced by introducing tensile strain. Therefore, Ge turns into direct bandgap material with the increase of the tensile strain. Transformation of Ge from indirect bandgap to direct bandgap provides an improvement in optoelectronic properties. In order to achieve a completely direct bandgap Ge, n-type doping can be introduced together with the tensile strain. The completely direct bandgap Ge matches to a wavelength of 1550 nm which has great significance in optical communication [25].

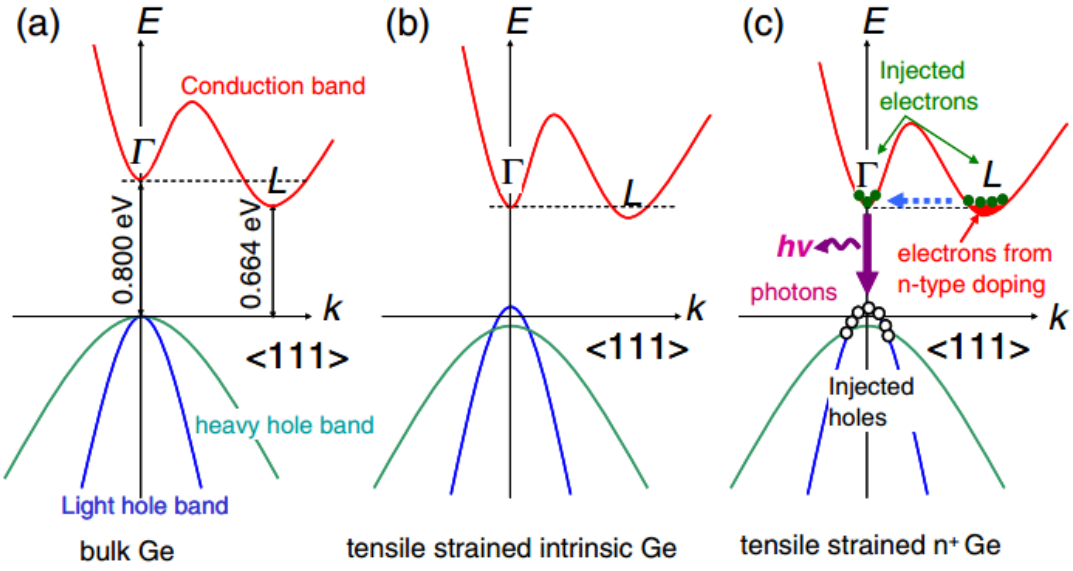

Figure 2.9: Band structure of bulk Ge (a), band structure of Ge where tensile strain is introduced (b), band structure of Ge where tensile strain and n-type doping are introduced together (c) [25].

During the direct growth of Ge on Si substrate, threading dislocations occur due to lattice mismatch (approximately 4%) between them. This high strain-related dislocation puts a limitation on device performance. In order to obtain high quality Ge-on-Si, various techniques can be adapted. One of these techniques is the

utilization of a graded buffer layer. Two different compositions of SiGe are grown on Si substrate to reduce the dislocation density. Figure 2.10 shows the cross section of gradually grown Ge photodiode.

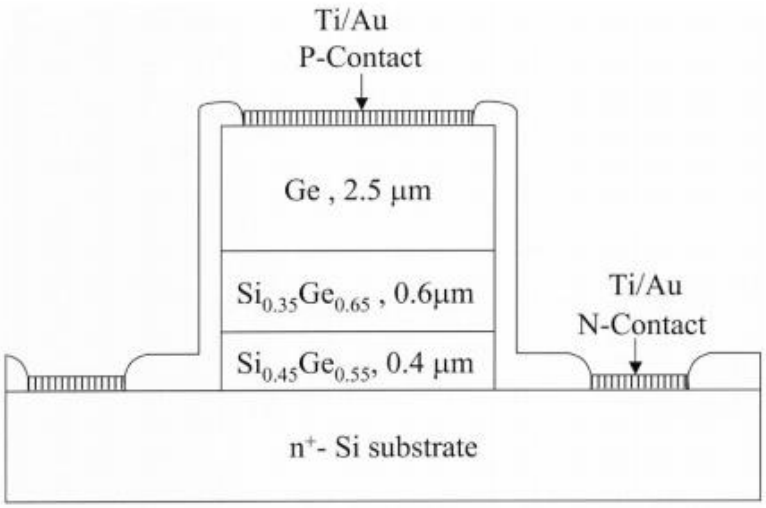

Figure 2.10: The cross section view of gradually grown Ge photodiode [26].

The primary limitation associated with the gradual growth of Ge-on-Si is that the thick graded layer makes the monolithic integration of photodiode arrays with ROICs difficult. As mentioned previously, the compatibility of Ge-on-Si photodetectors with ROICs is remarkable feature of these photodetectors.

Instead of growing thick Ge graded layer, threading dislocations can be reduced by growing a buffer layer at low temperature or inserting cycling thermal annealing. In the low temperature technique, a thin relaxed Ge buffer layer is directly grown on Si substrate without a graded buffer at a relatively low temperature compared to thick graded Ge buffer layer [27]. In the second technique, direct growth of Ge-on-Si is followed by cycling thermal annealing. When cyclic thermal annealing is combined with selective area growth, further improvement in dislocation density is achieved [28]. Figure 2.11 illustrates the general view of Ge photodiodes.

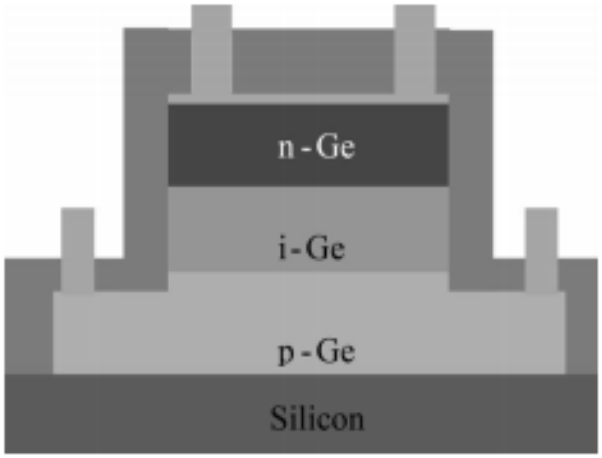

Figure 2.11: Cross sectional view of Ge photodetector [27].

Night vision is one of the most important application areas of Ge photodetectors. The demonstration of first successful monolithic integration of Ge photodetector with Si based ROICs is given in Figure 2.12. This detector is sensitive to visible and short wavelength infrared under moonless condition.

Figure 2.12: An image recorded by Ge photodetector under moonless condition [29].

2.2.2 Mercury Cadmium Telluride (HgCdTe)

Mercury Cadmium Telluride (MCT) is a direct bandgap material and zinc-blende alloy of HgTe and CdTe. Due to its semimetalic nature, $Hg_{1-x}Cd_xTe$ has a highly tunable bandgap adjustable by Cd composition x. Therefore, the bandgap of HgCdTe can be changed from less than 0.1 eV to more than 1.5 eV [30]. This feature makes it a desirable material for many applications over a wide IR range spanning from SWIR to VLWIR [31]. Figure 2.13 illustrates the bandgap energy and the corresponding cut-off wavelength of $Hg_{1-x}Cd_xTe$ varying according to Cd mole fraction, x.

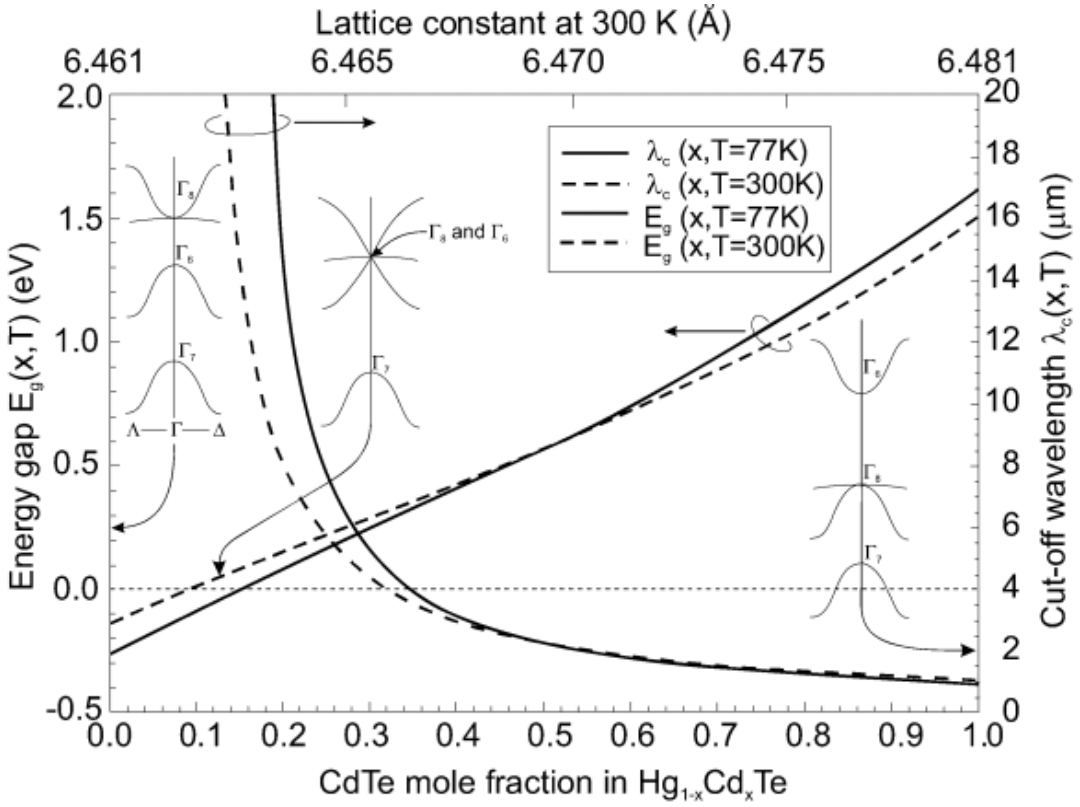

Figure 2.13: The bandgap energy and corresponding cut-off wavelength of $Hg_{1-x}Cd_xTe$ at 300 K [32].

There are several important observations that can be extracted by investigating Figure 2.13. Firstly, a small variation in Cd mole fraction results in a drastic increase or decrease in the relatively higher cut-off wavelengths. This situation causes a drastic reduction in growth uniformity of detector material. Secondly, the lattice constant of $Hg_{1-x}Cd_xTe$ demonstrates a minor change (from 6.461 to 6.481) in a wide

IR range. Therefore, it is possible to grow all compositions of $Hg_{1-x}Cd_xTe$ layer on the same substrate without any significant degradation. Traditionally high quality, lattice matched $Hg_{1-x}Cd_xTe$ can be grown on single crystal CdZnTe (CZT) substrate [33].

Although HgCdTe grown on CdZnTe provides the best quality material for detector production, it is very expensive and has limited size. For large size and high density FPAs, large area and high quality substrate is an important requirement. Therefore, alternative substrates such as Si, Ge, GaAs and GaSb are investigated. These substrates promise high crystal quality, large wafer size, low cost and ready availability. However larger lattice mismatch and coefficient of thermal expansion (CTE) difference between the HgCdTe and alternative substrates cause much larger defect densities than that of the HgCdTe layer grown on CdZnTe substrate. Figure 2.14 illustrates room temperature lattice constant and CTEs of alternative substrates.

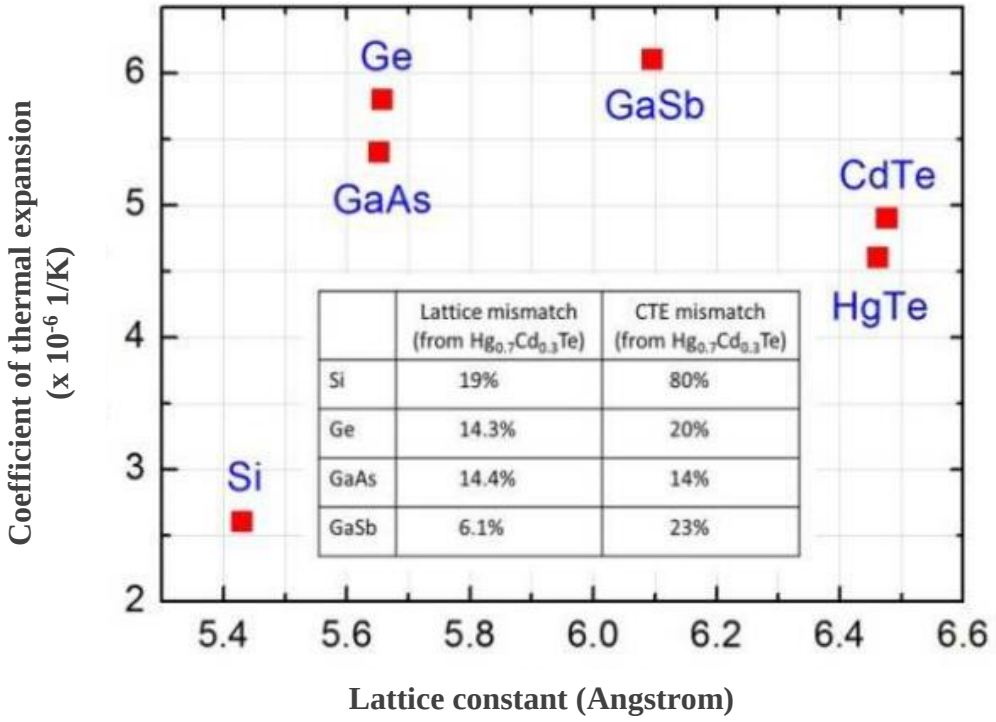

Figure 2.14: Lattice constant and CTEs for various semiconductors used as a substrate for HgCdTe growth [34].

As noted before, spectral sensitivity of HgCdTe detectors cover the extended SWIR spectral region up to 2.5 μm without sacrificing detector performance. Therefore, HgCdTe is a suitable detector material for the entire SWIR band applications. However, present IR detectors based on MCT require cryogenic cooling which increase the amount of power dissipation and make the system bulky and expensive [35].

2.2.3 Indium Gallium Arsenide (InGaAs)

Indium Gallium Arsenide ($In_xGa_{1-x}As$) material system has been of great interest for SWIR detector applications. One of the underlying reasons is the ability of InGaAs to operate at room temperature with high quantum efficiency. This feature makes it a suitable choice for SWIR imaging applications. InGaAs has also superior electrical properties (high electron mobility and velocity) and optical properties (direct bandgap and high absorption coefficient).

InGaAs is an alloy of Gallium Arsenide (GaAs) and Indium Arsenide (InAs). Both of the compound binaries are direct bandgap materials and $In_xGa_{1-x}As$ is also a direct bandgap material. GaAs itself can cover much of the same spectrum as Silicon (up to 0.9 μm) does. By adding indium to GaAs, the bandgap energy of InGaAs is lowered depending on indium mole fraction, x. Equation 2.1 is an empirical expression, which shows the change in energy bandgap depending on temperature and indium mole fraction, x [36].

$$E_g(x,T) = 0.42 + 0.625(1-x) - \left(\frac{5.8}{T+300} - \frac{4.19}{T+271}\right)10^{-4}T^2(1-x) - \frac{0.000419}{T+271}T^2 + 0.475(1-x)^2 \quad (2.1)$$

where T is temperature in K.

Figure 2.15 illustrates the energy bandgap of $In_xGa_{1-x}As$ material system according to indium mole fraction, x at 300 K. As it can be seen from Figure 2.15, the temperature dependent bandgap of the alloy can be adjusted from 1.4 eV for pure GaAs (x=0) down to 0.35 eV for pure InAs (x=1).

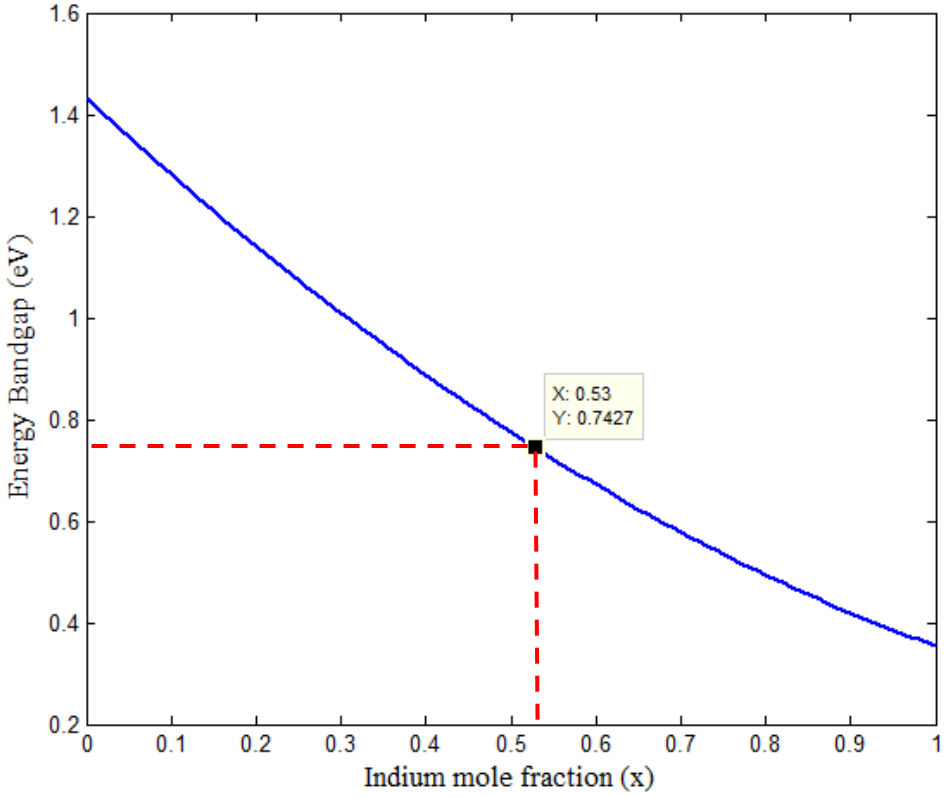

Figure 2.15: The bandgap energy of $In_xGa_{1-x}As$ versus In mole fraction, x at 300 K.

The cut-off wavelength of $In_xGa_{1-x}As$ can be calculated by making use of Equation 1.9. Fig 2.16 shows the cut-off wavelength of this material according to In mole fraction, x at 300 K. As it can be seen from Figure 2.16, the cut-off wavelength of the alloy can be adjusted from 3.5 μm for pure InAs (x=1) down to 0.87 μm for pure GaAs (x=0).

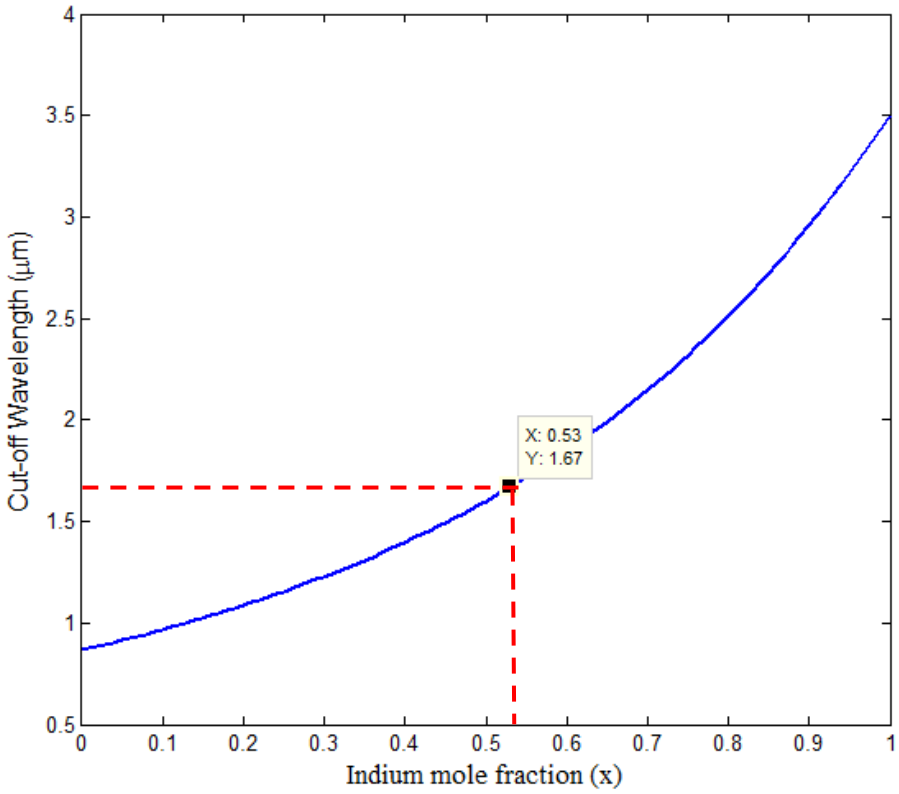

Figure 2.16: The cut-off wavelength of $In_xGa_{1-x}As$ versus In mole fraction, x at 300 K.

In order to obtain high quality epilayers, the lattice constant of the InGaAs should be lattice matched with the substrate. The lattice parameter of the alloy changes between 5.6533-6.0583Å. The lattice constant of InGaAs with 53.2% indium has the same lattice constant value with InP substrate. The lattice constant of InGaAs alloy can be expressed as [37]

$$a = 6.0583 - 0405(1 - x)\ (\text{Å}) \tag{2.2}$$

Figure 2.17 illustrates the variation in the lattice constant of InGaAs with the In mole fraction, x. $In_xGa_{1-x}As$ with 0.53 In composition grows lattice matched on InP substrate. The energy bandgap and the corresponding cut-off wavelength of $In_{0.53}Ga_{0.47}As$ are 0.75 eV and 1.7 μm, respectively [38].

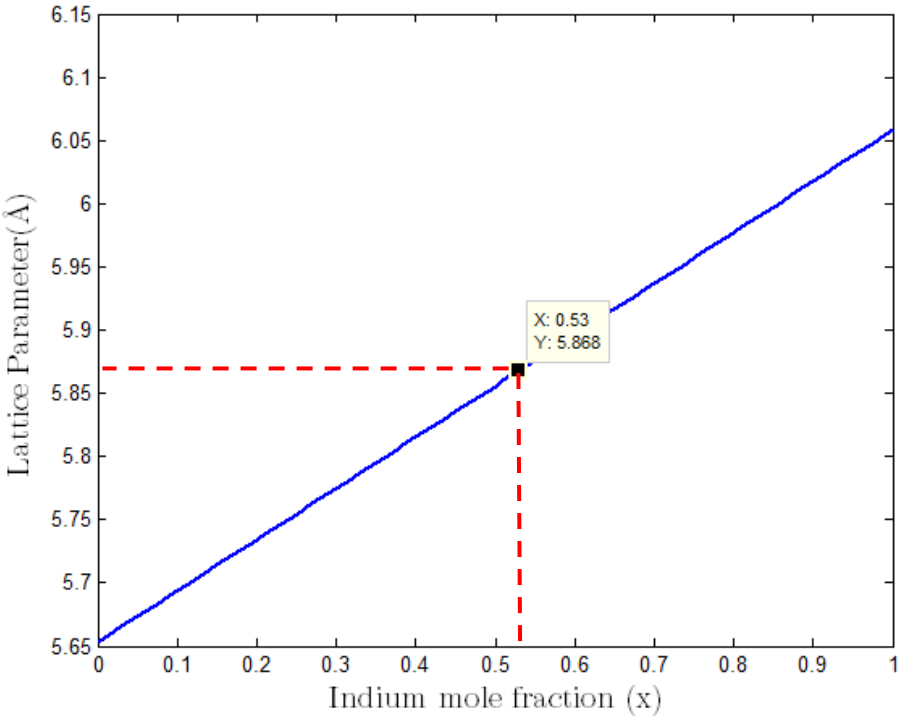

Figure 2.17: The variation of the lattice constant of $In_xGa_{1-x}As$ with the In mole fraction, x.

$In_{0.53}Ga_{0.47}As$ lattice matched to InP substrate has been sufficiently developed for decades. By increasing the In mole fraction, the cut-off wavelength can be extended up to 3.4 µm. There are many reports in literature which realize the cut-off wavelength up to 2.7 µm [24,25,41]. As the content of In increases and the cut-off wavelength gets longer, detector performance parameters such as dark current and quantum efficiency start to degrade. Extended wavelength SWIR detectors have excess dark current components due to misfit dislocations when compared with the lattice matched SWIR detectors. In order to reduce these dislocations due to lattice mismatch, there is a report in literature that suggests step grading rather than continuous grading [42]. Figure 2.18 shows spectral response of three InGaAs detectors with 1.7, 2.2 and 2.5 µm cut-off wavelengths. As it can be clearly seen from Figure 2.18, InGaAs with 1.7 µm cut-off wavelength is a convenient choice when only the spectrum of night glow of the sky is taken into account [4].

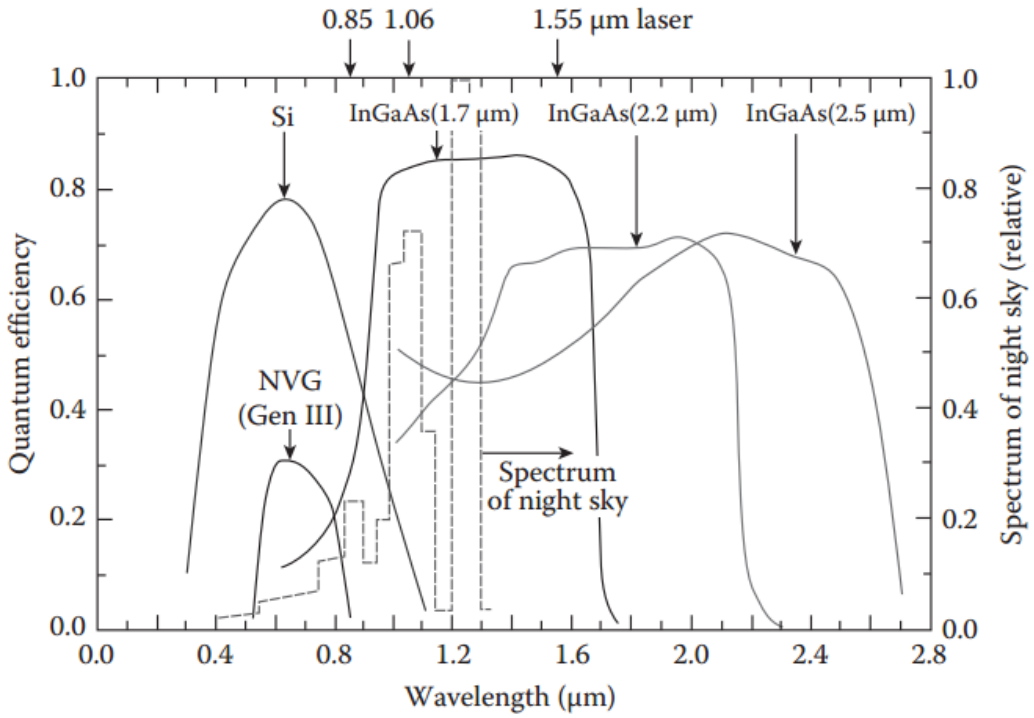

Figure 2.18: Quantum efficiency of InGaAs with 1.7 μm, 2.2 μm and 2.5 μm cut-off wavelength [4].

While determining the detector materials for SWIR imaging applications, it is crucial to consider the relative tradeoffs of the key parameters such as performance parameters (responsivity, dark current etc.), reliability, camera size, weight, power consumption, and technology platform readiness. The most widely used material systems for SWIR band detection are HgCdTe and InGaAs. In the sense of night vision imaging, airglow plays an important role in moonless sky. Figure 2.19 illustrates the quantum efficiency of HgCdTe and InGaAs along with the airglow spectrum.

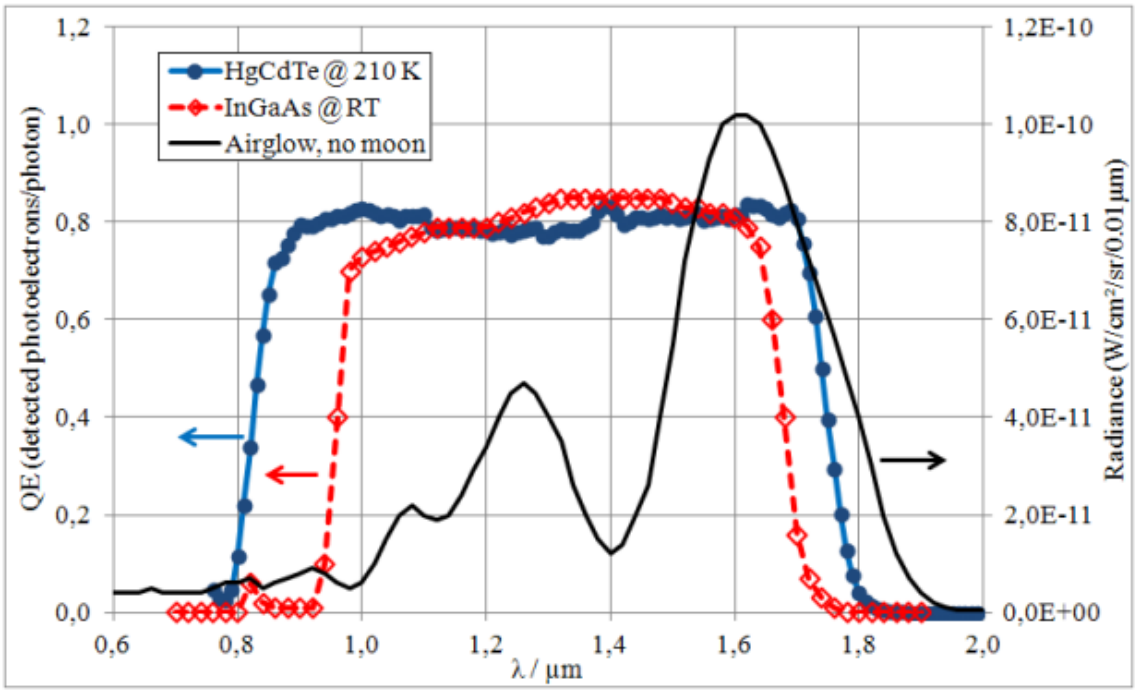

Figure 2.19: Quantum efficiency of HgCdTe and InGaAs along with airglow spectrum [30].

Even though HgCdTe detector has wider cut-on and cut-off wavelength interval when compared with lattice matched InGaAs (0.9-1.7 µm) detector, both of them benefit from the maximum radiation of airglow spectrum. Cut-on wavelength of InGaAs detector is determined by the energy bandgap of InP substrate which is 1.35 eV, corresponding to the cut-off wavelength of 920 nm. For backside illuminated detectors, InP substrate absorbs radiation with wavelengths below 920 nm before it reaches InGaAs region. In order to increase the quantum efficiency towards to the end of visible range, InP substrate can be removed. Therefore, InGaAs active region responds to visible wavelengths [43]. Figure 2.20 shows the amount of enhancement in the spectral response of InGaAs active material.

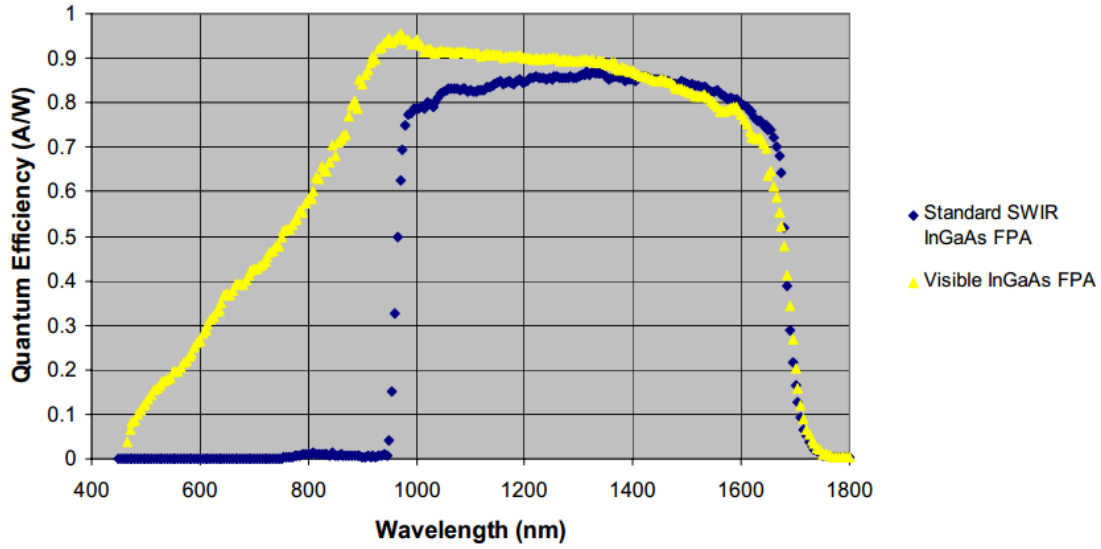

Figure 2.20: Quantum efficiency improvement of lattice-matched InGaAs detector [44].

In conclusion, InGaAs detectors provide the lowest production cost among all other material systems that can be utilized in SWIR band [45].

2.3 Basics of InGaAs SWIR Detectors

As mentioned in Chapter 1, instead of using photoconductor (PC), photovoltaic (PV) detector structures are preferred for IR detectors since electric field is created internally. As PV detectors, the p-i-n photodiode is utilized mostly as an alternative to p-n photodiode. A p-i-n diode is a special p-n junction with an intrinsic or lightly doped semiconductor layer sandwiched between heavily doped p+ and n+ type semiconductor layers. Figure 2.21 illustrates the structure of p-i-n diode and energy band diagram under reverse bias conditions.

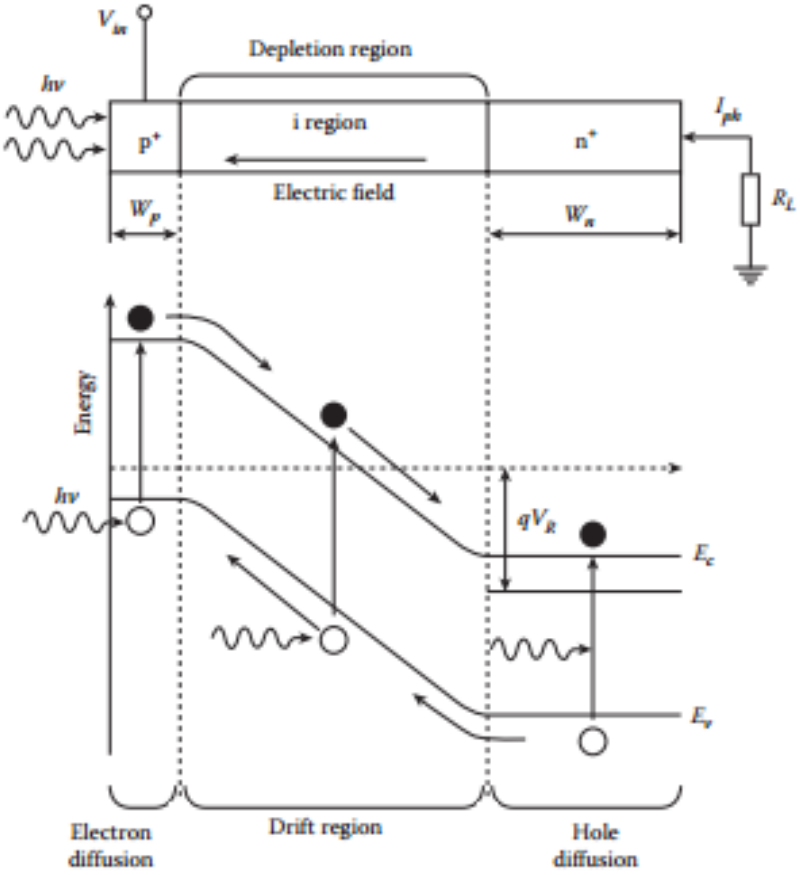

Figure 2.21: The structure of the p-i-n photodiode and energy band diagram under reverse bias conditions [4].

When the p-n junction is constructed, intrinsic layer called as absorber layer is completely depleted. Due to high resistivity in the intrinsic layer and low resistivity in the surrounding heavily doped p+ and n+ region, almost the entire reverse bias applied the structure drops across the absorption layer. There are two important characteristics of the p-i-n photodiode.

- The depletion region is completely defined by the absorber layer
- The E-field is constant across the absorber layer.

As seen from Figure 2.22, while the p-i-n photodiode has a constant E-field profile across the depletion region, p-n junction has peak E-field at the junction and decreasing E-field profile to the end of depletion region in the n and p side. Therefore, the p-i-n diode has a higher response speed even though it has a larger

depletion region. With the thickness of the absorption layer, both the quantum efficiency and the response speed of a p–i–n photodiode can be optimized. In order to achieve high quantum efficiency, absorber layer width should be large and to achieve high response speed the width should be small [46]. There is a tradeoff between response speed and quantum efficiency.

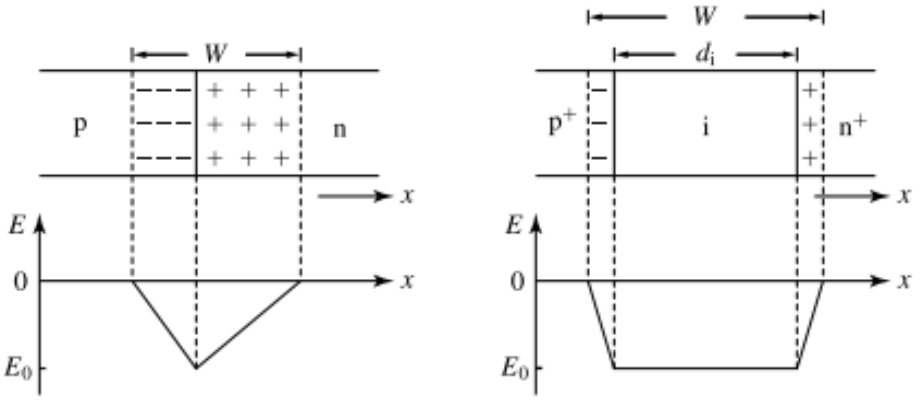

Figure 2.22: Electric field profile of p-n diode (left) and p-i-n diode (right) [46].

2.4 Device Structure of InGaAs SWIR Detectors

In this section, the features of both mesa and planar structures are briefly discussed. $In_{0.53}Ga_{0.47}As$/InP based p-i-n photodiodes are constructed typically in the planar structure.

2.4.1 Mesa Type

In the mesa type pixel arrangement, p-type and n-type layers are realized during the growth. Each pixel is formed by etching process which can be dry or wet. After the etching process, pixels are isolated from each other. The epitaxial layer and the schematic cross section of mesa type p-i-n photodiode are given in Figure 2.23 and SEM image of mesa type pixels is given in Figure 2.24.

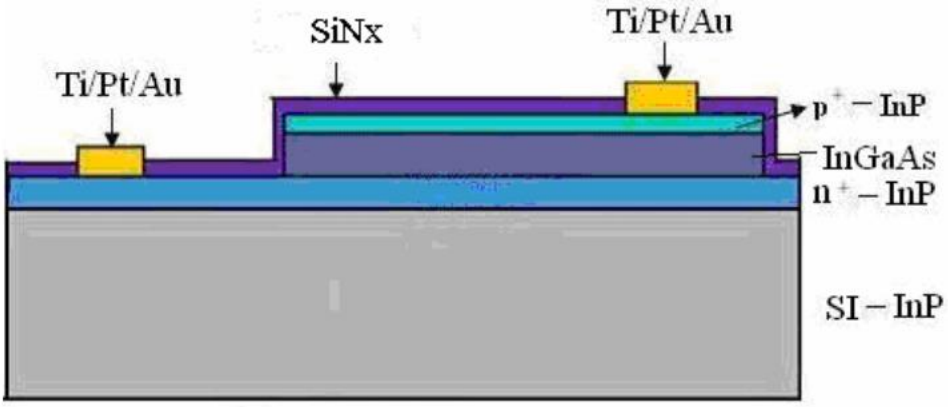

Figure 2.23: The schematic cross section of mesa type p-i-n InGaAs photodiode [47].

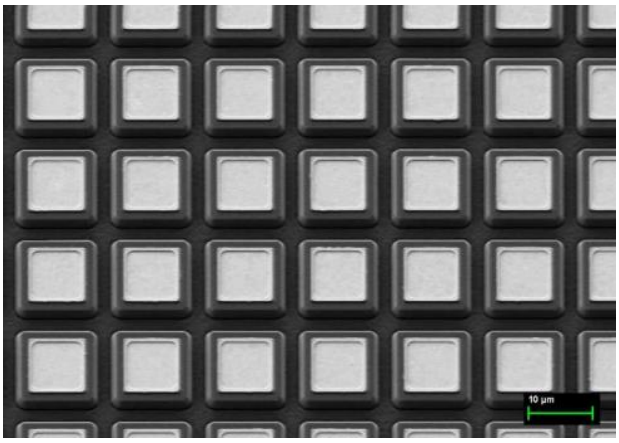

Figure 2.24: SEM image of mesa type pixels [47].

Besides mesa type p-i-n photodetector structure is easy to fabricate, it has a lot of advantages such as high reproducibility, uniformity and being compatible for dual color applications.[48]. However, etching process induces dangling bonds on side walls which are responsible for the surface leakage current. These dangling bonds may lead to unstable dark currents [49]. In order to minimize dark current related to surface and increase the stability of dark current, the passivation of side walls plays a critical role. Dielectric materials such as SiO_2, SiN_x, and polyimide can be utilized for passivation of photodiode surface.

2.4.2 Planar Type

In the planar type arrangement, p-type region is formed by diffusion, generally Zn diffusion, through the InP cap layer after or during the growth. The most important advantage of this type of detectors is that the junction is automatically protected when it is formed. Figure 2.25 illustrates the epitaxial layer and the schematic cross section of planar type p-i-n InGaAs photodiode.

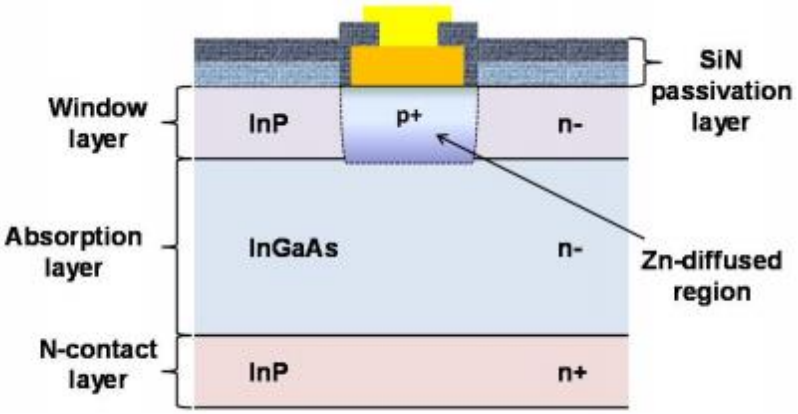

Figure 2.25: The schematic cross section of planar type p-i-n InGaAs photodiode [50].

Since the thickness of absorber layer and depletion layers determine critical performance parameters such as quantum efficiency and response time, Zn diffusion process should be optimized carefully. It is easier to achieve lower dark current level in planar type compared with the mesa type as the pixels are buried in the planar type in contrast to isolated pixels in mesa types. While mesa type suffers from surface leakage current due to dangling bonds, planar type does not. However, planar type suffers from cross talk between the pixels since the pixels are not totally isolated and planar type is not compatible with dual color applications.

2.5 State of Art SWIR Photodetectors

Over the last years, IR detector research groups have been working on different detector structures in order to decrease the dark current. They also focus on smaller pixel pitch and larger format FPAs in order to have advantages for applications related to long range observation and to have more compact product.

In 2015 Sofradir, which has transferred the imaginary activities from the III-V Lab, has reported a VGA format of 640x512 pixels with a pitch of 15 µm p-i-n photodiodes grown by Metal Organic Vapor Phase Epitaxy (MOVPE) on 4-inch n^+ type InP substrates. Planar type is preferred as the detector structure, and p-type in the n-InP window layer is created by Zn diffusion. In order to obtain more stable and reliable sensor, SiN is utilized as the passivation layer. Then, detector array is flip-chip bonded to ROIC with indium bumps based reflow process. After the hybridization process, InP substrate is thinned down to a few hundred nanometers to extend the cut-on wavelength. The photodiode array can detect the light between 0.4 and 1.7 µm. Furthermore, SiO_2/TiO_2 materials are utilized as antireflection coating that provides transmission on spectral band of interest. Dark current as low as 17 fA is obtained under 0.2 V reverse bias voltage at an ambient temperature of 20 ^oC and the operability of pixels is 99.97% [19]. Figure 2.26 illustrates the process of indium bumps.

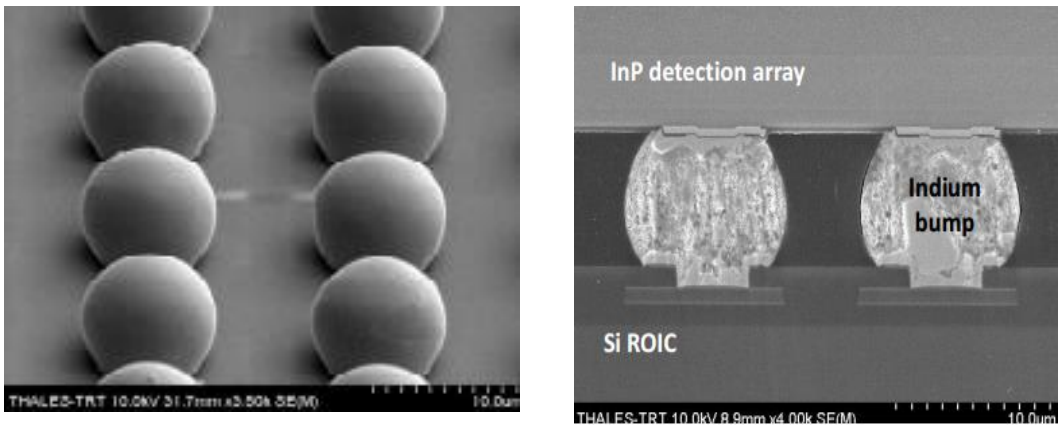

Figure 2.26: 15 µm pitch indium bumps after reflow process and indium bump connection between the FPA and ROIC [39].

In this study, the origin of dark current is also investigated in more detail. In order to provide lower dark current, considerable effort was made to obtain high quality material. When the material quality is not optimized, a high defect density exists in the depleted region, where charge carriers contributing to the dark current can be generated. In that case, dark current is linked to a Shockley Read Hall (SRH) mechanism and they suggest that dark current is proportional to the photodiode area. When the material quality is optimized, defect densities decrease in the depletion region and SRH mechanism becomes negligible. In that case, dark current is due to the diffusion of minority carriers under low reverse bias voltage and they suggest that dark current is proportional to the photodiode perimeter [52]. Figure 2.27 illustrates that dark current is proportional to pixel diameter whatever the pixel pitch is.

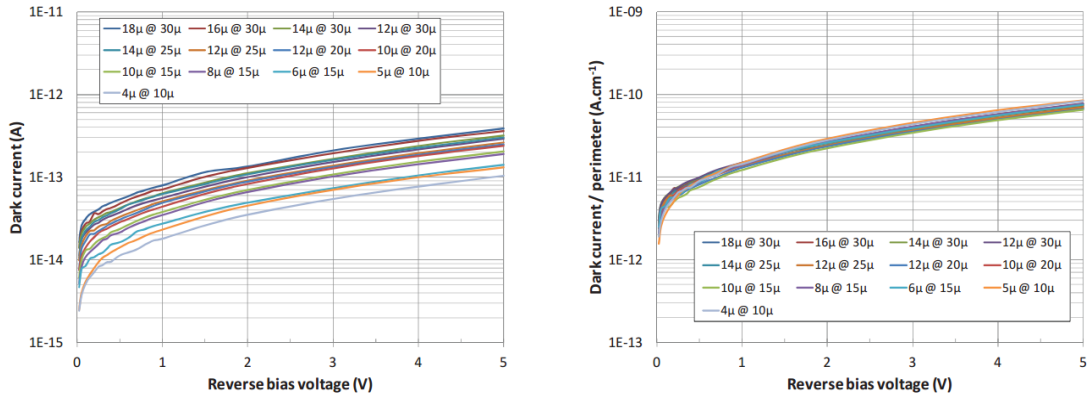

Figure 2.27: The dark current of pixels with different pixel diameters and the same pixel pitch under reverse bias voltage (left), and the dark current of pixels with different pixel diameters and the same pixel pitch under reverse bias voltage, which are divided by pixel perimeter (right) [53].

In 2016, Fraunhofer Institute for Applied Solid State Physics (IAF) has demonstrated the first 640x512 SWIR camera which makes use of the signal gain of avalanche photodiodes (APDs). In order to achieve very thin layers with abrupt interfaces, which are required for the optimization of APD structure, MBE growth technique is preferred. Due to advantages over planar type, mesa type pixel arrangement is utilized as the detector structure. The pixels are formed by HBr-based inductively coupled plasma (ICP). This dry-etching process is followed by the consecutive wet

etch process. Then, a suitable dielectric passivation is applied to minimize surface leakage current. Detector array is flip-chip bonded with a specific ROIC developed at AIM. After the hybridization process, InP substrate is removed by mechanical grinding and then wet-etching is performed. Figure 2.28 shows a part of detector array after the removal of the etch stop layer.

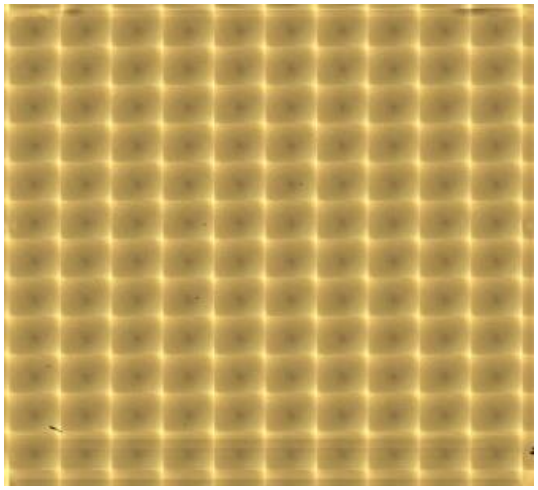

Figure 2.28: A part of 640x512 FPA with 15 μm pitch after thinning the etch stop layer [54].

While research on the optimization of APDs was going on [55] at IAF, the standard p-i-n photodiode was characterized and the state of art dark current densities below 10 nA/cm^2 at 200 K were achieved for the mesa type detector in 2013. Figure 2.29 shows the dark current densities for two different p-i-n photodiodes at various operating temperatures. The difference between the dark current densities of pixel with the area of 400x400 μm^{2}and 40x40 μm^2 results from the non-perfect passivation of mesas.

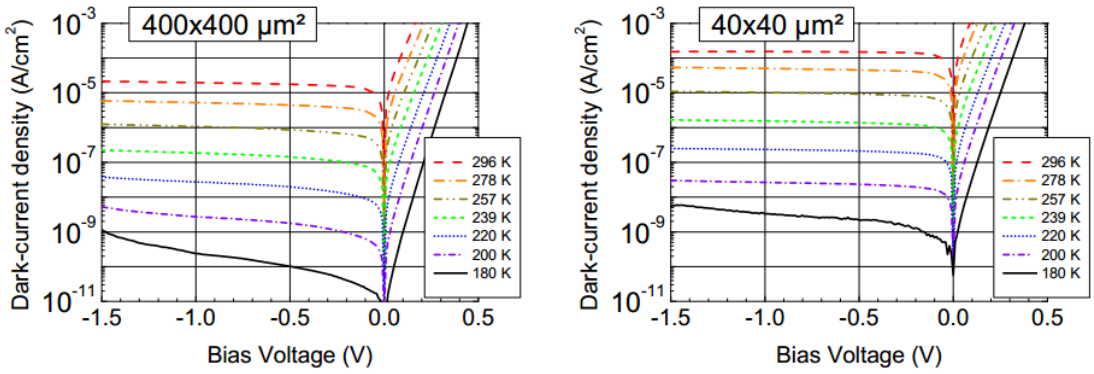

Figure 2.29: The dark current densities of pixel with the area of 400x400 µm^2 (left) and 40x40 µm^2 (right) at various temperatures [56].

In SWIR imaging, the detection of low photon flux is a requirement. When the standard p-i-n photodiodes are used, they should have high responsivity and low dark current for the detection of low photon flux. In order to cope with low photon flux in SWIR band region, IAF developed SWIR detector making use of APDs internal signal gain. Figure 2.30 illustrates an image recorded by the standard InGaAs SWIR detector and an image recorded by InGaAs based APDs SWIR detector. Both scenes were illuminated indirectly with a halogen lamb.

Figure 2.30: An image recorded by a standard InGaAs SWIR camera (left) [57] and by an InGaAs based APDs SWIR camera (right)[58].

CHAPTER 3

FABRICATION AND CHARACTERIZATION OF InGaAs SHORT WAVELENGTH INFRARED FPAs

This chapter presents the investigation of the characteristics of the pixels of a large format (640x512) FPA with 15 μm pixel pitch together with the characterization of test detectors with larger areas. The discussion starts with the growth and fabrication processes of the FPA. The following section is devoted to the investigation of the dominant dark current component of the large area test detectors. The results extracted from dark current modeling are compared with Deep Level Transient Spectroscopy (DLTS) measurement results. Finally, the characteristics of the FPA pixels with small (15 μm) pitch are presented.

3.1 Growth of the Device Epilayer Structure

Molecular Beam Epitaxy (MBE) is an epitaxial growth technique which was utilized in this work for the growth of epilayers. The epilayer design and growth of the device structure were conducted by the other members of the Quantum Devices and Nanophotonics Research Group of the Electric and Electronics Engineering Department of METU.

3.1.1 The Basics of Molecular Beam Epitaxy

Molecular beam epitaxy (MBE) is an ultra-high vacuum (~10^{-11}-10^{-10}) technique for growing epitaxial layers on crystalline substrates. Due to high vacuum environment, it is quite possible to produce high quality single crystal materials. Ultra-high

vacuum is preserved by various vacuum pumps such as cryopump, ion pump and liquid nitrogen cryopanelling. The vacuum system includes a stainless-steal growth chamber, buffer chamber and a load lock module for transferring the wafer to and from air. Epilayer growth is conducted in high vacuum growth chamber. Growth chamber contains effusion cells, substrate heater, in-situ characterization tools and system monitoring equipment. Figure 3.1 shows the Riber Epineat system.

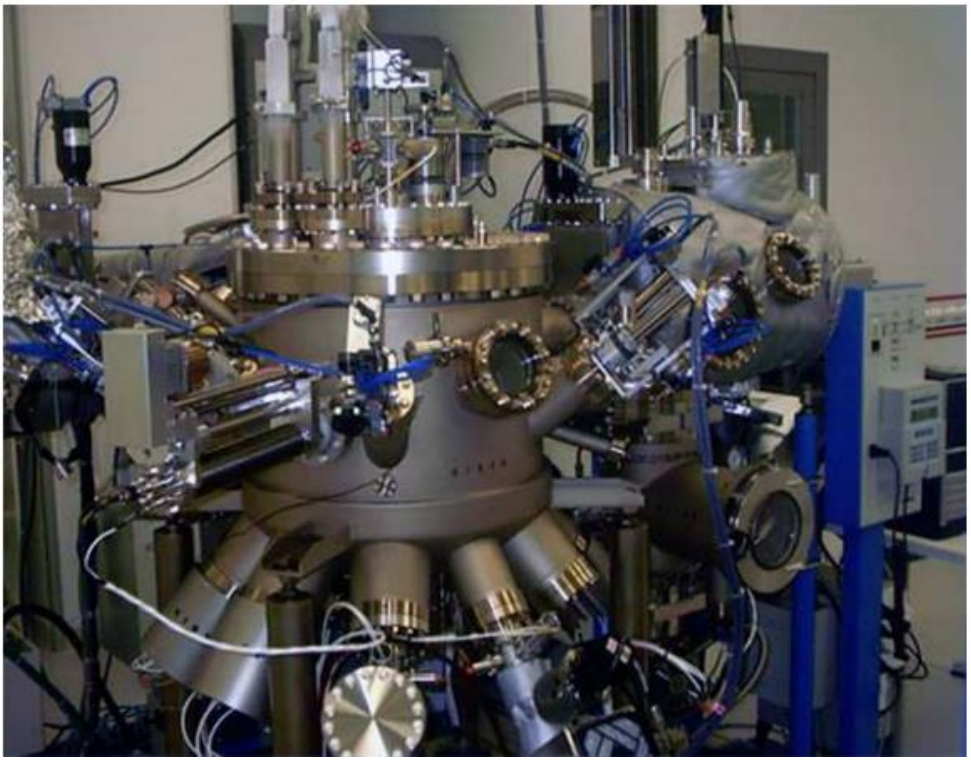

Figure 3.1: Riber Epineat system in Quantum Devices and Nanophotonics Research Laboratory, METU.

The effusion cells are co-focused on the substrate heater to provide flux uniformity. They are resistively heated and temperatures are precisely controlled with the feedback received by the thermocouples in the effusion cells. There are shutters in front of each effusion cell and substrate heater. During the growth, they operate in the sequence determined previously. The various growth calibrations are conducted in order to achieve desired composition of compound semiconductors. As a result of these growths, a relation between fluxes and growth rate is established for the

purpose of using in the following growths. Before starting the crystal growth, flux is controlled by a flux gauge measuring the beam equivalent pressure.

3.1.2 Detector Epilayer Structure

The epilayer structure employed in this study is given in Figure 3.2. This structure is in the form of a heterojunction p-n diode which consists of $In_{0.53}Ga_{0.47}As$ absorbing layer between an n-type (Si) doped InP and a p-type (Be) doped $In_{0.48}Al_{0.52}As$ layers. This structure is different than that of the standard lattice matched SWIR InGaAs detector in the sense that the p-type layer is $In_{0.48}Al_{0.52}As$ instead of InP. These layers are lattice matched to each other with the given compositions. A p-type (Be) doped $In_{0.53}Ga_{0.47}As$ contact layer on p-$In_{0.48}Al_{0.52}As$ cap layer is added to design in order to have better ohmic contact. The absorber $In_{0.47}Ga_{0.53}As$ layer is unintentionally doped. This design also contains an etch stop layer to stop backside wet etching during substrate removal.

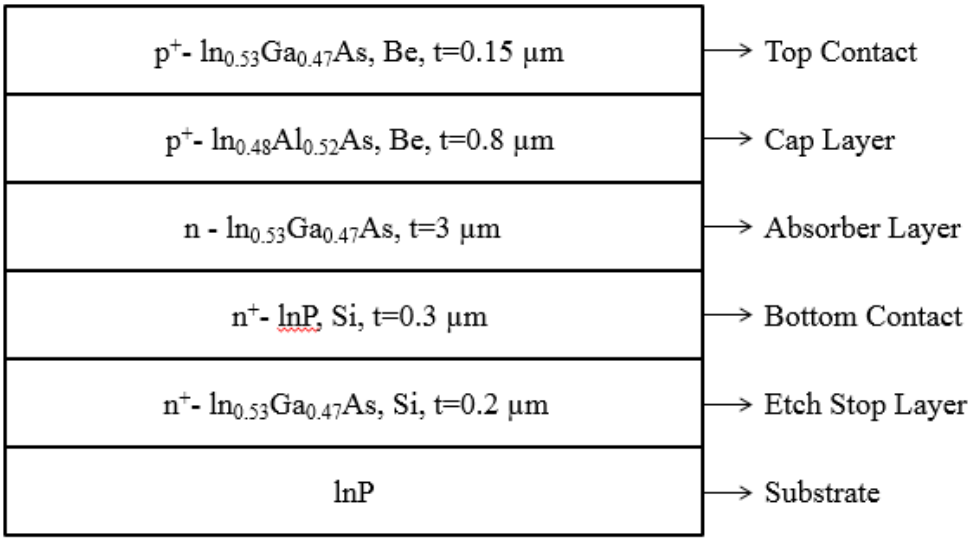

Figure 3.2: The epilayer structure utilized for fabrication of FPA.

The above structure was grown with MBE on 4-inch semi insulating InP substrate using the Riber Epineat system located at the Quantum Devices and Nanophotonics Research Laboratory.

3.2 Fabrication of Large Format (640x512) Focal Plane Array

The fabrication steps of the FPA are illustrated in Figure 3.3. The first step of the fabrication is forming the alignment marks which have a crucial role in sustaining the rest of process steps. After the formation of the alignment marks, deposition of the ohmic contact metals is performed on top of the p-type InGaAs layer. If the alignment marks are formed by the deposition of metals, p-type contact and alignment mark steps can be done at the same time. Ohmic contact formation is followed by the etching process of p-InGaAs, p-InAlAs and n-InGaAs absorber layer in order to form an island on the n^+-InP bottom contact layer. This etching process is followed by the bottom ohmic contact metal deposition and annealing. After ohmic contact metallization, pixels are defined by wet etching. After etching tests with different chemicals, uniform mesa sidewalls and reasonably small amount of underetch is achieved by using a confidential solution. Figure 3.4 depicts the mesa etch profile using this etchant.

After several passivation tests, mesa sidewalls are passivated with the most effective passivation material. In order to reach both n-type and p-type contacts, openings in the passivation layer are formed by etching. Figure 3.5 illustrates the formation of passivation openings located at the middle of p-type ohmic contacts.

Following the passivation, indium bumps are formed in order to perform vertical connection between the FPA and the ROIC. Prior to indium bumping, under bump metallization (UBM) is performed for two main reasons. UBM acts as a barrier and blocks indium diffusion to FPA pixels. UBM also increases the adhesion between pixels and indium bumps. Indium bumps are formed by e-beam evaporation.

After the formation of indium bumps, detector array is flip-chip bonded to MT6415CA read out integrated circuit (ROIC) which is designed by Mikro-Tasarim Ltd. for SWIR InGaAs detectors. This CTIA ROIC has the noise level less than $5e^-$ in the very high gain mode at 300 K [59].

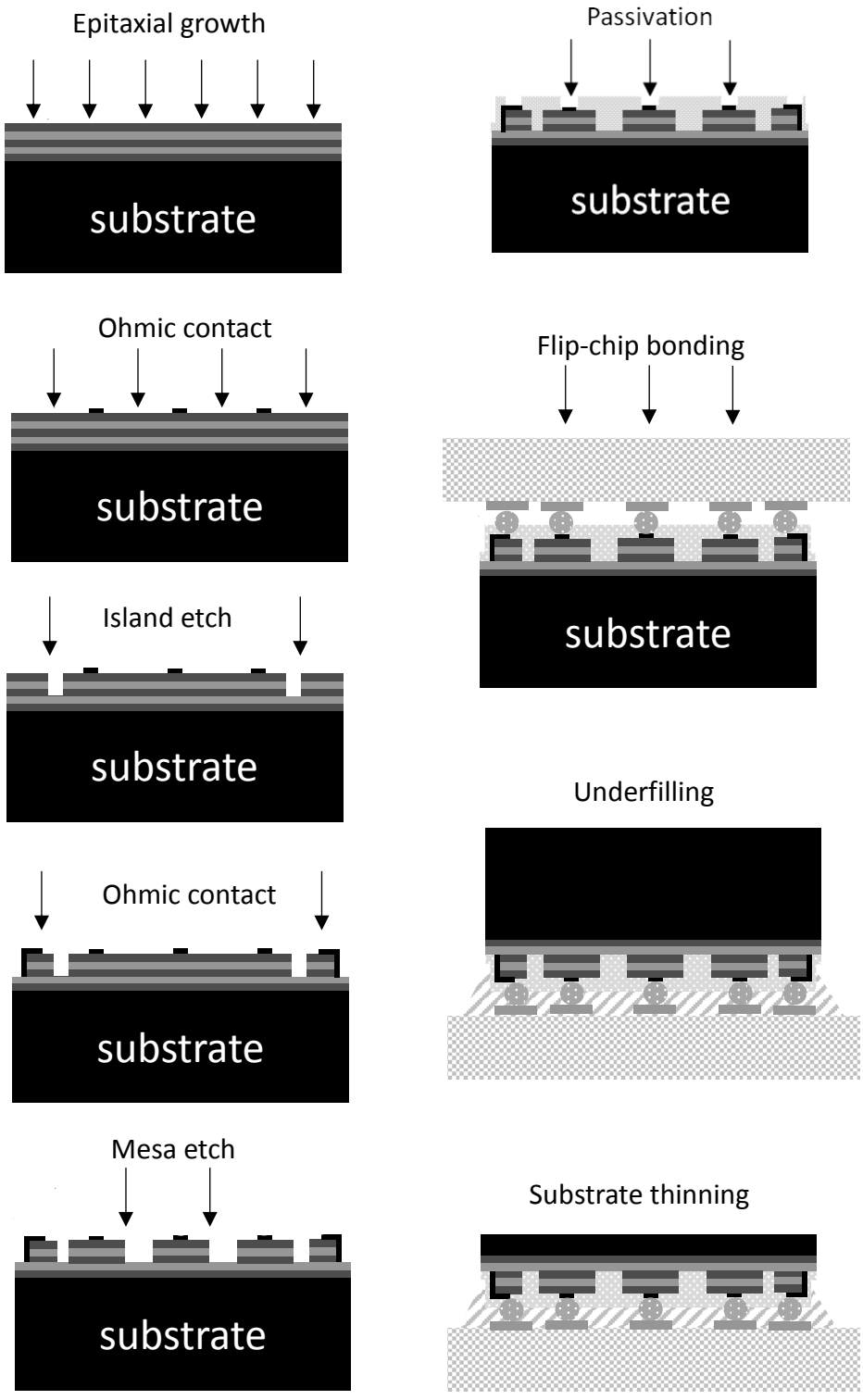

Figure 3.3: Illustration of fabrication steps for a detector.

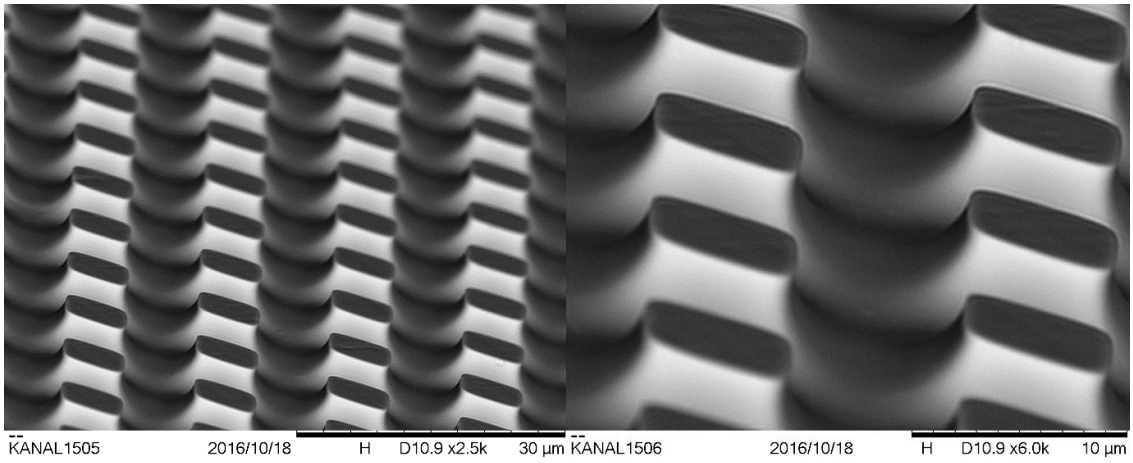

Figure 3.4: SEM images of mesa etch profile.

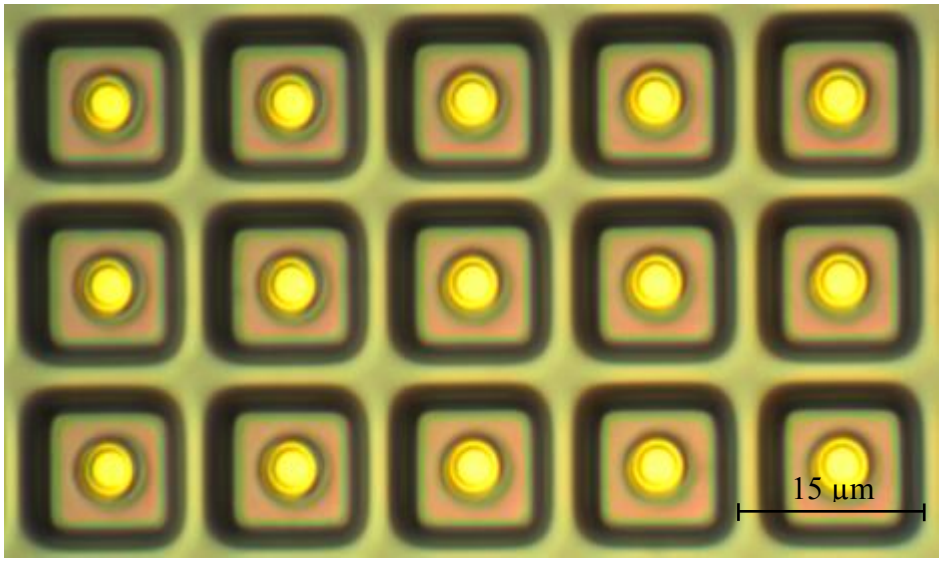

Figure 3.5: The top view of mesas after the formation of passivation opening on top of the pixels.

After hybridization process, a special underfill epoxy is injected into the gap between ROIC and FPA in order to improve the mechanical strength. Underfilling is followed by substrate thinning. There are several reasons for thinning or completely removing InP substrate. First of all, stress between FPA and Si based ROIC is reduced by thinning substrate to several µm thickness. Additionally, diffraction of incoming radiation resulting from thick and unpolished backside of detector is prevented.

Finally, as discussed in Section 2.2.3, responsivity of the detector can be extended to visible range by completely removing the substrate. Figure 3.6 shows the picture of the FPA after integration with the ROIC and substrate thinning.

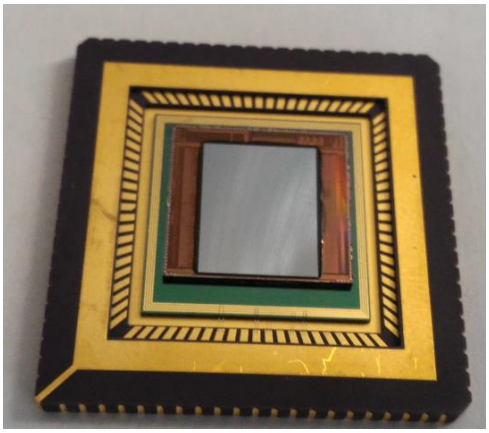

Figure 3.6: The photograph of the FPA after integration with ROIC and substrate thinning.

3.3. Device Characterization and Modeling

Lower dark current is an important issue to realize imaging at night because of small amount of photon flux in the SWIR band. In this section, characterization results of test detectors and test pixels identical to FPA pixels are presented. First, the dominant dark current component of the test detectors was investigated by fitting a model including diffusion, generation-recombination (G-R) and shunt currents to experimental data. Next, the dominant trap level suggested by the fitting was investigated by employing DLTS measurement technique as a further study. Finally, the I-V characteristics and dark current modeling results of the test pixels are presented and discussed.

3.3.1. I-V Characterization of Test Detectors

With the purpose of dark current modeling, test detectors with various areas (125x125 μm^2, 100x100 μm^2 and 75x75 μm^2) were fabricated. The test detectors have the same epilayer structure with FPA and are subjected to quick process steps

including ground etching, ohmic contact deposition and mesa formation by wet etching.

In general, dark current of a p-n diode is the sum of two major components: surface current and bulk generated current. The bulk component of the dark current includes diffusion current, generation-recombination current, shunt current and tunneling current. The surface component may include generation-recombination current, surface leakage current and additional tunneling currents [42]. There is no considerable contribution of tunneling current above 220 K up to the reverse bias voltage of -2 V in the samples utilized within the scope of this thesis.

Diffusion Current

Diffusion current results from diffusion of thermally generated minority carrier towards the depletion region. Diffusion current can be expressed as follows

$$I_{diff} = I_s(e^{qV/kT} - 1) \tag{3.1}$$

where q is the electron charge, k is the Boltzmann constant, T is the junction temperature, and V is the applied bias voltage. I_s is the saturation current (for a long diode) given as [60]

$$I_s = qA\left(\sqrt{\frac{D_n}{\tau_n}}\frac{n_i^2}{N_A} + \sqrt{\frac{D_h}{\tau_h}}\frac{n_i^2}{N_D}\right) \tag{3.2}$$

where A is the device area, τ_n and τ_p are the electron and hole lifetimes, N_A and N_D are acceptor and hole densities, n_i is the intrinsic carrier concentration, and D_n and D_p are the electron and hole diffusion coefficients. Diffusion coefficients can be calculated by using the Einstein relation

$$\frac{D}{\mu} = \frac{kT}{q} \tag{3.3}$$

where μ is the carrier mobility.

Generation-Recombination (G-R) Current

The G-R current may be the dominant dark current component in diodes with high defect or impurity density. This current results from generation and recombination process of EHPs through the traps introduced by the defects or impurities. If the trap level is close to the midgap position, the G-R current can be approximated as [61]

$$I_{g-r} = \frac{qn_i AW}{\tau_{eff}}(e^{qV/2kT} - 1) \tag{3.4}$$

where τ_{eff} is the effective G-R lifetime, V is the applied bias voltage and W is the depletion region width. Depletion region width introduces the major voltage dependency of the G-R current and can be expressed as

$$W = \sqrt{\frac{2\varepsilon_s(V_{bi} - V)}{q}(\frac{1}{N_A} + \frac{1}{N_D})} \tag{3.5}$$

where ε_s is the permittivity and V_{bi} is the built-in voltage, which is expressed as

$$V_{bi} = \frac{kT}{q} ln \frac{N_A N_D}{n_i^2} \tag{3.6}$$

In the above expression, N_A and N_D are acceptor and hole densities and n_i is the intrinsic carrier concentration.

Surface Generation-Recombination (G-R) Current

The G-R current related to surface is due to the formation of dangling bonds and Fermi-level pinning. The proportionality of surface G-R current can expressed as

$$I_{g-r}(surface) \propto \sqrt{V_{bi} - V}\exp(^{-E_g}/_{2kT}) \tag{3.7}$$

where V is the applied bias voltage.

Ohmic Leakage or Shunt Current

Shunt current may originate from non-ideal passivation of pixels and threading dislocations introduced during the epilayer growth. Shunt current is given as

$$I_{shunt} = \frac{V}{Rsh} \tag{3.8}$$

where R_{sh} is the shunt resistance of the diode and V is the applied bias voltage.

Temperature Dependency of Dark Current

Under low reverse bias voltages, diffusion current and G-R current may be the major dark current components indicating strong temperature dependency. Under reverse bias voltage ($|V| \gg 2kT/q$), the ratio of the g-r current to the diffusion current can be expressed as [42]

$$\frac{I_{g-r}}{I_{diff}} = \frac{Wn\tau_p}{L_p n_i \tau_{eff}} \tag{3.9}$$

If weak temperature dependency of L_p, τ_p and τ_{eff} are taken into consideration, the ratio of g-r current to diffusion current can be simplified as fallow

$$\frac{I_{g-r}}{I_{diff}} \propto {}^{1}/_{n_i} \propto \exp({}^{E_g}/_{2kT}) \tag{3.10}$$

At high temperatures, diffusion is likely to be the dominant dark current mechanism due to strongest temperature dependency. When the temperature starts to decrease, the diffusion current decreases faster and the G-R current may become the dominant dark current mechanism.

As mentioned above, dark current consists of bulk and surface currents. Therefore it is possible to express dark current as follows

$$I_{dark} = I_b + I_s \tag{3.11}$$

$$I_{dark} = J_b A + J_s P \tag{3.12}$$

where P and A stand for the perimeter and area of a pixel, respectively. In order to separate bulk and surface currents, Equation 3.11 is divided by pixel perimeter as given follows

$$I_{dark}/_{P} = J_b A/P + J_s \tag{3.13}$$

In order to illustrate negligible contribution of surface current to total dark current for large pixel areas (125x125 μm^2,100x100 μm^2 and 75x75 μm^2), a study was carried out on test detectors which have different areas (and different area/perimeter ratios). The slope of the characteristic in Figure 3.7 identifies the bulk current component. The intercept stands for the surface current exhibiting negative value as a result of being too small to be detected in this process. This characterization work suggests that most of the dark current of the detectors with areas larger than 75x75 μm^2 is bulk generated.

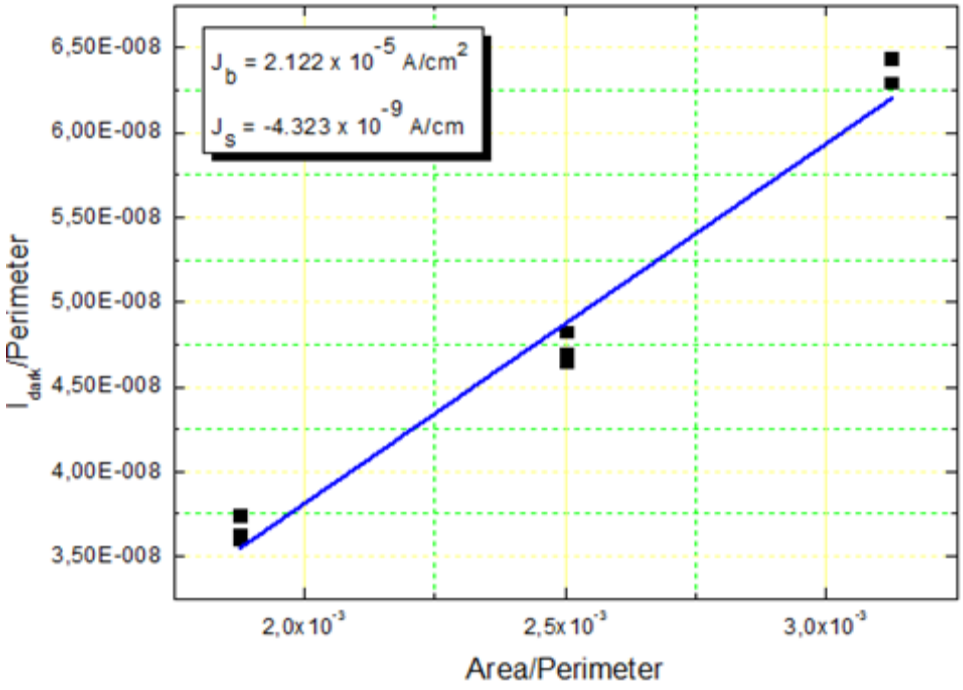

Figure 3.7: Linear fit for large detector areas (125x125 μm^2, 100x100 μm^2 and 75x75 μm^2) at 100 mV reverse bias and 300 K, which indicates that dark current is dominated by bulk current.

For modeling of dark current, the test detector with 125x125 μm^2 area is utilized. In order to separate dark current into components, a model which consists of diffusion, G-R and shunt currents is adopted. This model includes only bulk related g-r current as given in Equation 3.14.

$$I_{dark} = I_{diff} + I_{g-r} + I_{shunt} \tag{3.14}$$

I_{diff}, $I_{g\text{-}r}$ and I_{shunt} are rearranged as given in Equation 3.15, 3.16 and 3.17.

$$I_{diff} = C_{diff}(e^{qV/kT} - 1) \tag{3.15}$$

$$I_{g-r} = C_{g-r}\sqrt{V_{bi} - V}\ (e^{qV/2kT} - 1) \tag{3.16}$$

$$I_{shunt} = C_{sh}\, V \tag{3.17}$$

where C_{diff}, $C_{g\text{-}r}$ and C_{sh} are the voltage independent parameters.

By using curve-fitting, the model established in Equation in 3.14 is fit to experimental results. Figure 3.8 illustrates that the detectors display G-R dominated dark current behavior at 300 K. This result is consistent with those reported for lattice matched $In_{0.53}Ga_{0.47}As$/InP photodiodes in the literature [8,9]. R_{shunt} is 0.7 GΩ. By making use of Equation 3.4 and 3.5 effective G-R lifetime is calculated as 1.5 μs.

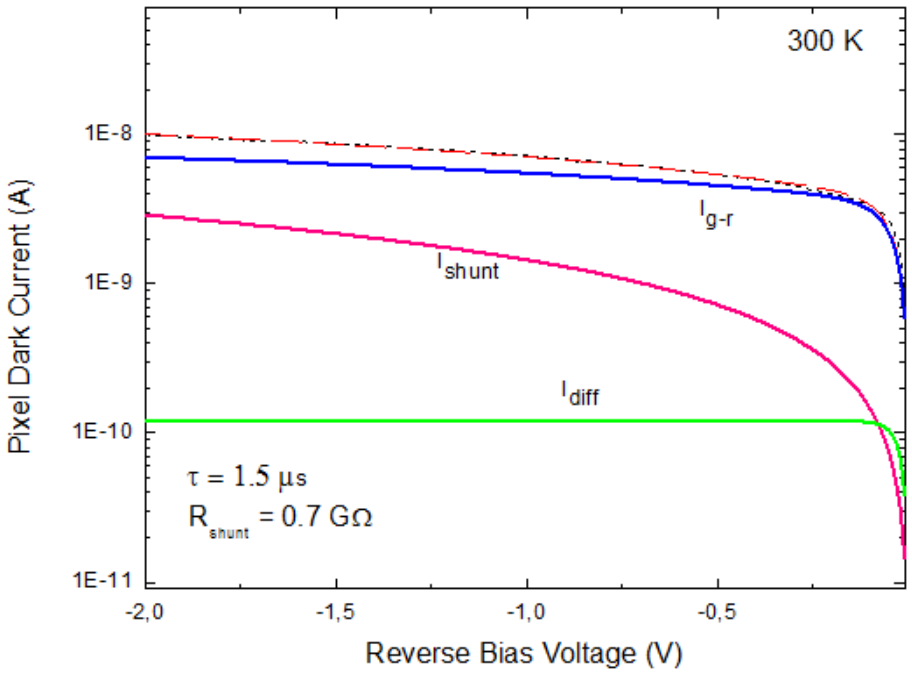

Figure 3.8: The dark current modeling of test detector with 125x125 μm^2 pixel area at 300 K.

In order to determine the activation energy of the G-R current, curve fitting is applied at temperatures between 300 K and 240 K. As mentioned previously, the G-R current indicates a temperature dependency proportional to intrinsic carrier concentration, n_i. Figure 3.9 illustrates the G-R component of the dark current at various temperatures. The activation energy of G-R dominated dark current is obtained by making use of exponential dependency of intrinsic carrier concentration on temperature. Figure 3.10 illustrates the fitting to obtain activation energy. The activation energy related to G-R component of dark current obtained as 0.497 eV. The activation energy of $E_g/1.5$ suggests that the performance of test detector is considerably degraded by defects and impurities located at the depletion region.

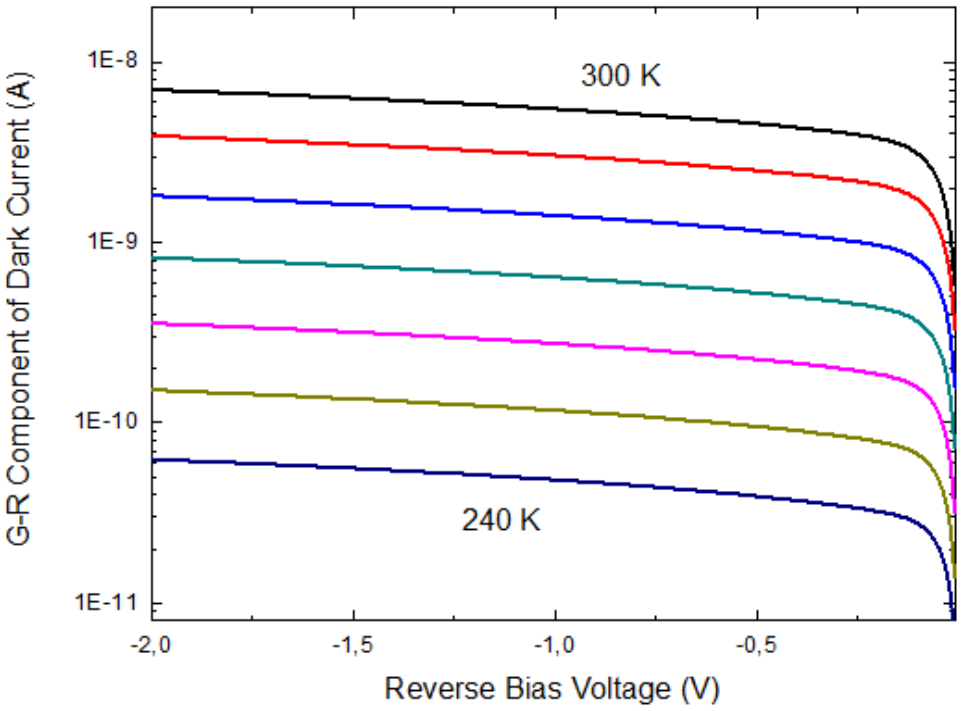

Figure 3.9: The G-R component of dark current for test detector with 125x125 μm^2 pixel area at various temperatures.

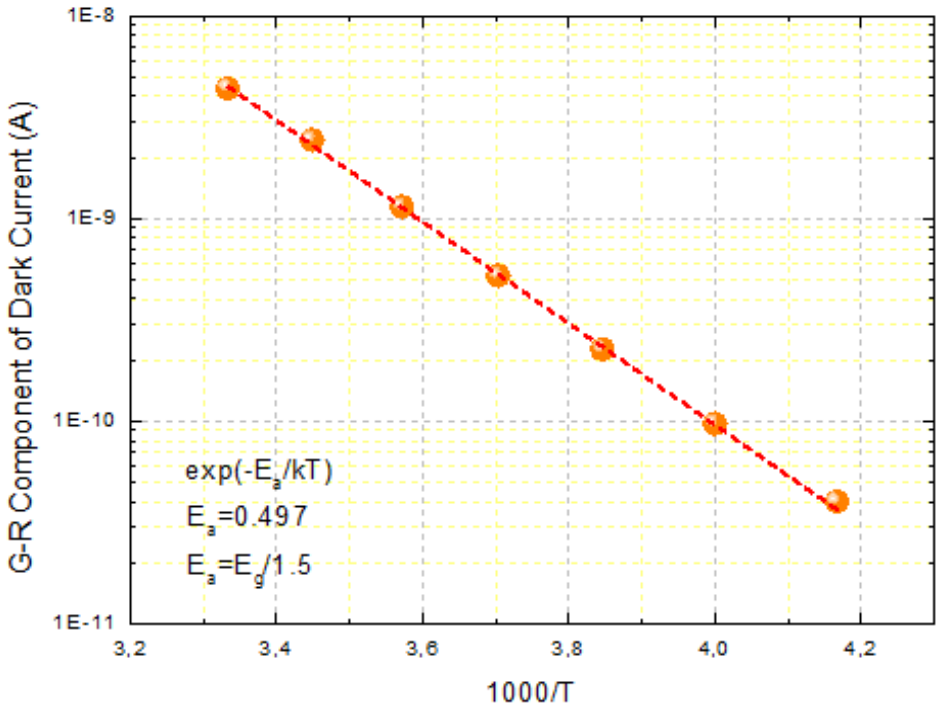

Figure 3.10: The estimation of G-R current activation energy by fitting under 100 mV reverse bias voltage.

Figure 3.11 illustrates the variation of effective G-R lifetime (τ_{eff}) with temperature. The activation energy is extracted as 0.17 eV by using fitting. This result shows a trap located at the energy level of 0.17 eV with respect to the E_i. Further wok on identifying the properties of this trap is presented in section 3.3.2.

Figure 3.12 demonstrates the variation of shunt resistance with respect to temperature. Ohmic leakage current is created by dislocations in the semiconductor and non-ideal passivation of mesa sidewalls. Since the test detectors have mostly bulk generated dark current, it is likely that this shunt leakage current completely originates from threading dislocations in the semiconductor. The activation energy of $E_g/1.8$ being close to $E_g/2$ indicates that shunt current increases almost in proportional to n_i.

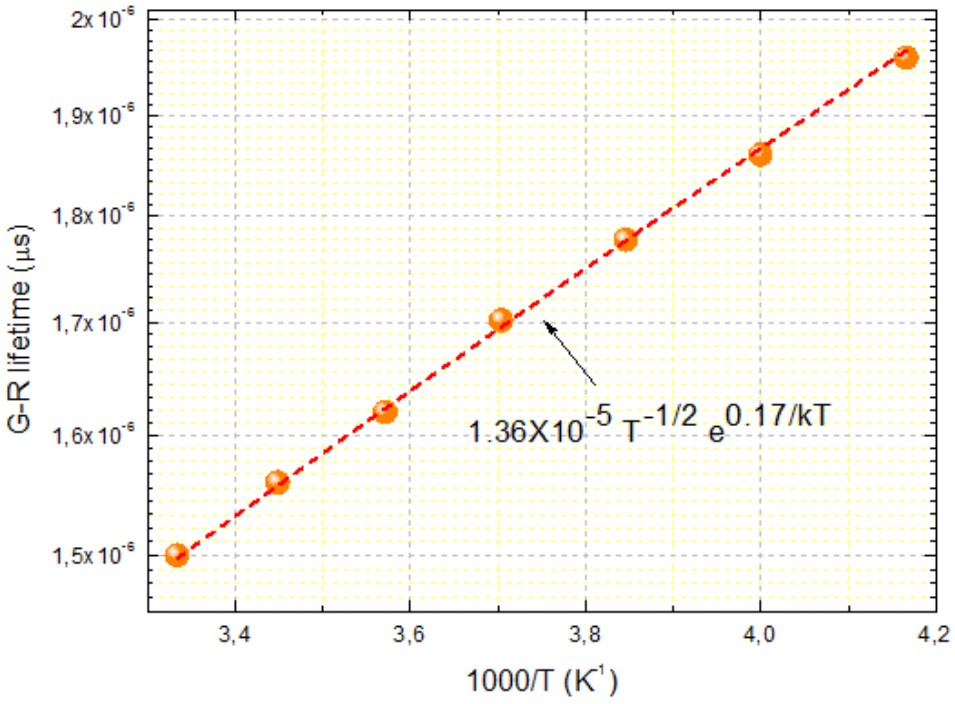

Figure 3.11: The variation of effective G-R lifetime with respect to the temperature.

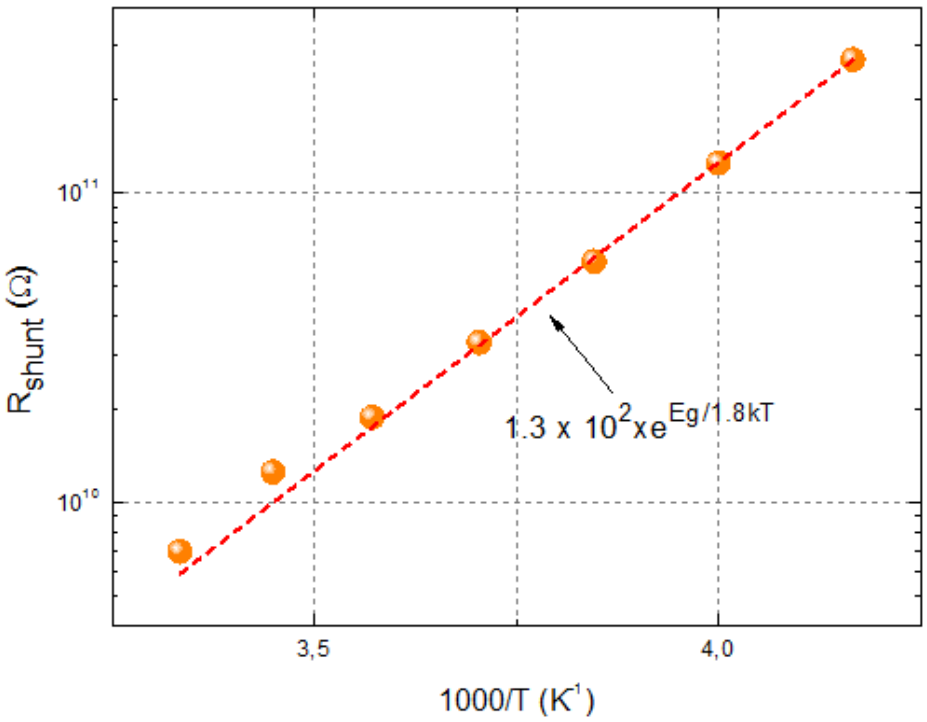

Figure 3.12: The variation of shunt resistance with respect to the temperature.

3.3.2. C-V Measurements and Trap Characterization

Traps in semiconductor layer have a significant effect on dark current. Therefore, the determination of these traps in semiconductor layer is required to improve the growth conditions further. Before the investigation of these traps by Deep Level Transient Spectroscopy (DLTS), C-V measurement is conducted in order to estimate the doping density of n-type absorber layer.

3.3.2.1. C-V Measurements

C-V measurement is employed to determine the doping density of the absorber layer. In the case of uniformly doped p^+-n junction, the doping density of n-type doped layer can be calculated by using Equation 3.18.

$$N_D = \frac{2}{q\varepsilon_s A^2 \frac{d(1/C^2)}{dV}} \tag{3.18}$$

where N_D is the n-type doping density, q is the electron charge, ε_s is the permittivity of material, A is the area of pixel, C is the depletion capacitance and V is the bias voltage. Figure 3.13 illustrates C-V and $1/C^2$-V curves of the test detector. By extracting the slope from $1/C^2$-V plot, the doping density of n-type absorber layer is calculated as 2.22 x10^{15} cm^{-3}.

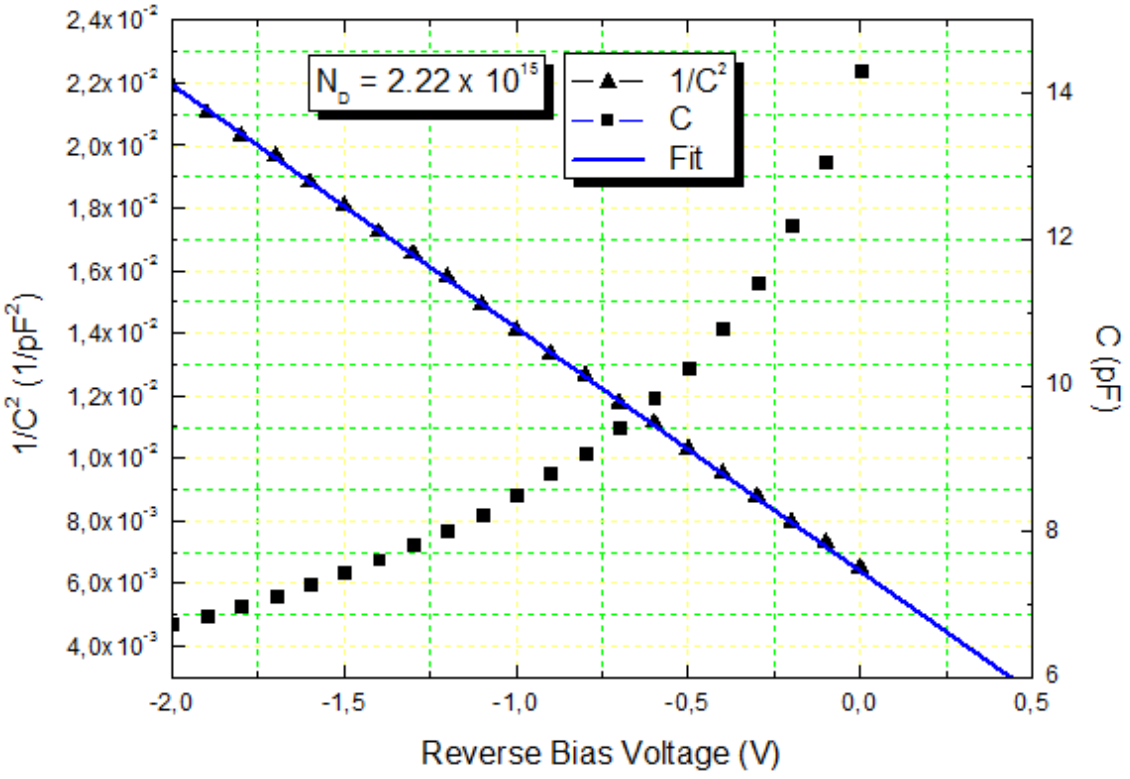

Figure 3.13: The C-V and $1/C^2$-V curves of a test detector with the area of 125x125 μm^2.

3.3.2.2. Deep Level Transient Spectroscopy (DLTS)

In order to achieve lower dark currents, the origin of dark current should be investigated accurately. The defects have a crucial effect on the dark current. In this point, defects can be classified into two main groups as shallow level and deep level defects. Shallow level defects are introduced by doping which is conducted

intentionally to obtain p-type and n-type materials. Deep level defects are caused by unwanted dopants and the crystalline defects such as vacancies and dislocations, which occur during the growth. These traps control the generation-recombination rate and the lifetime of charge carriers.

Deep Level Transient Spectroscopy (DLTS), as introduced by Lang in 1974, is a method to investigate the existing traps in the semiconductor [64]. In this method, high-frequency capacitance transient measurement is performed as a function of temperature. The properties of traps in the semiconductor can be extracted from DLTS measurement results. The capacitance measurement results in negative and positive peaks, which correspond to the majority and minority traps. The peak amplitude determines the trap concentration. As a result of DLTS measurement, activation energies of traps, electron or hole-capture cross sections for each trap and trap densities can be obtained.

DLTS measurements were conducted on a test detector with an area of 200x200 μm^2 by another member of the Quantum Devices and Nanophotonics Research Laboratory. DLTS measurement was performed in the temperature range of 10-350 K for various delay times. Positive peaks and negative peaks are attributed to minority and majority traps, respectively in an n-type semiconductor. Since the absorber layer is n-type material, the majority carrier trap is referred to as an electron trap, and the minority carrier trap as a hole trap.

As a result of the DLTS measurement, one minority trap is observed. The DLTS spectra and Arrhenius plot of this minority trap is given in Figure 3.14 and 3.15, respectively. This minority trap has an activation energy of 0.52 eV, density of $9.87x10^{14}$ cm^{-3} and capture cross-section of $8.78x10^{-15}$ cm^2. This minority trap is located at E_i+0.15 eV at 300 K, which is close to the trap level extracted from the fit of effective G-R lifetime.

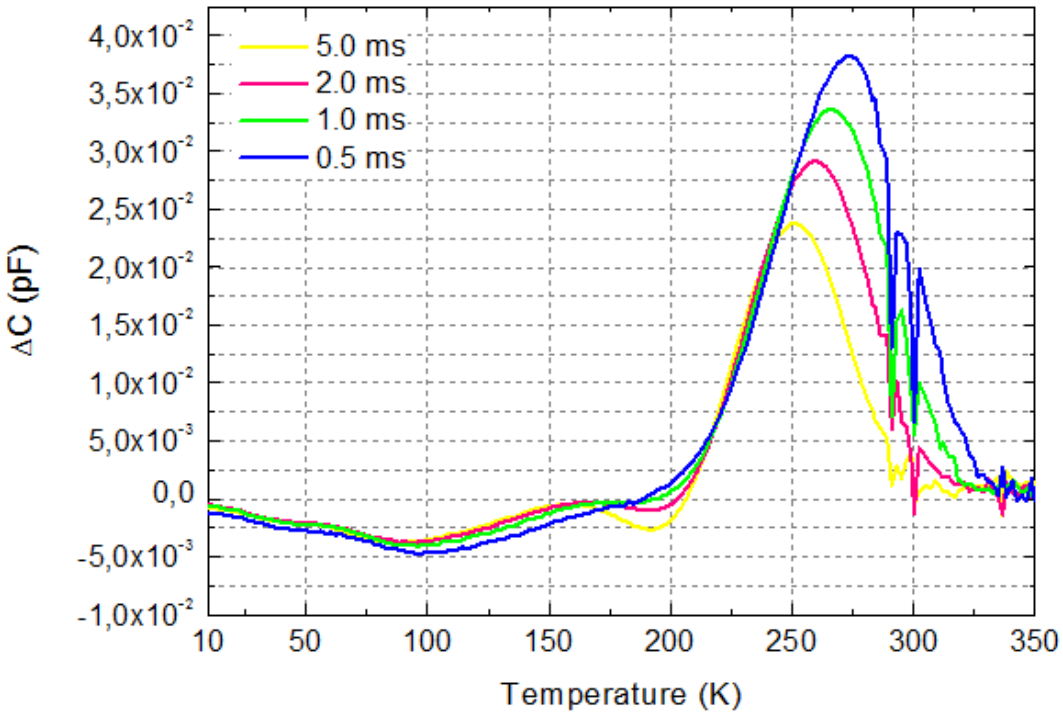

Figure 3.14: DLTS spectra of the test detector for various delay times at temperatures between 10 K and 350 K.

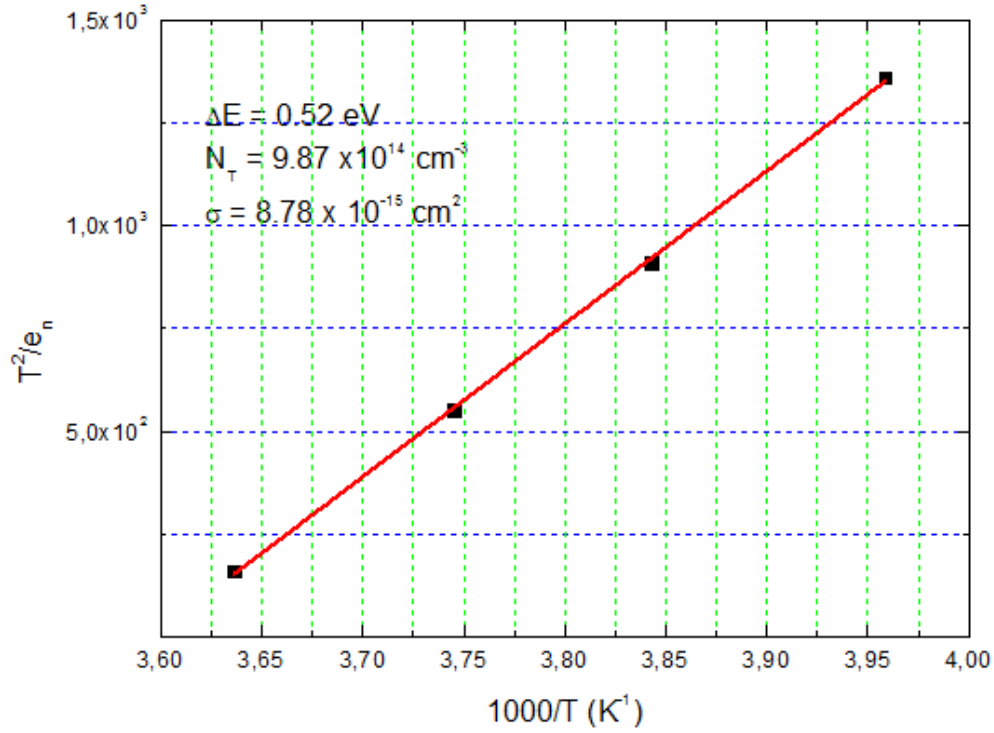

Figure 3.15: Arrhenius plot and the properties of the observed minority carrier trap.

The G-R lifetime can mathematically be expressed as follows [41]

$$\tau = \frac{1}{\sigma_t \vartheta_{th} N_T} e^{E_T - E_i / kT} \tag{3.19}$$

where σ_t is the capture cross-section, ϑ_{th} is the thermal velocity, N_T is the trap density and E_T is the trap level with respect to intrinsic level, E_i. By inserting the DLTS results of minority trap into Equation 3.19, the G-R lifetime is found as 1.9 μs at 300 K. The effective G-R lifetime extracted from dark current modeling is obtained as 1.5 μs at the same temperature. The G-R lifetimes obtained from modeling and DLTS measurement have a reasonable agreement, which are in the same order of magnitude with those reported for $In_{0.53}Ga_{0.47}As/InP$ in the literature [65]. The results also suggest that the minority carrier trap observed through the DLTS measurements is responsible for the G-R current dominating the dark current of large area test detectors.

3.3.3. I-V Characterization of Test Pixels

In this section, characterization results of the test pixels are presented. These pixels are identical to the FPA pixels and they undergo the same process steps with that of FPA on the same die. In order to make the electrical contacts to the test pixels, they are flip-chip bonded with a fan-out substrate. After flip-chip bonding, fan-out hybrid is mounted on an alumina substrate, and electrical connections are established between fan-out and alumina by wire bonding. Figure 3.16 shows a fan-out hybrid placed on the alumina substrate.

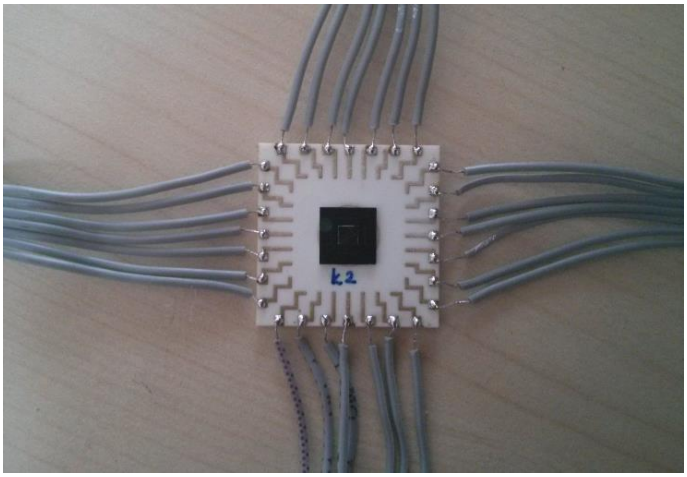

Figure 3.16: Test pixel array hybridized with a fan-out and placed on alumina substrate.

In order to determine the dominant dark current component, a model which is composed of diffusion (I_{diff}), generation-recombination (I_{g-r}) and shunt (I_{shunt}) currents is adopted. Figure 3.17 shows that the test pixels display G-R dominated dark current behavior at 300 K. The G-R lifetime and R_{shunt} is obtained from the fitting as 65 ns and 4.6 GΩ, respectively.

In order to obtain the activation energy of G-R current, dark current modeling is conducted at the temperature from 320 K to 250 K. Figure 3.18 shows the results of fitting work implemented to obtain the activation energy. The resulting activation energy was obtained as 0.55 eV which is larger than that of the test detectors with larger areas.

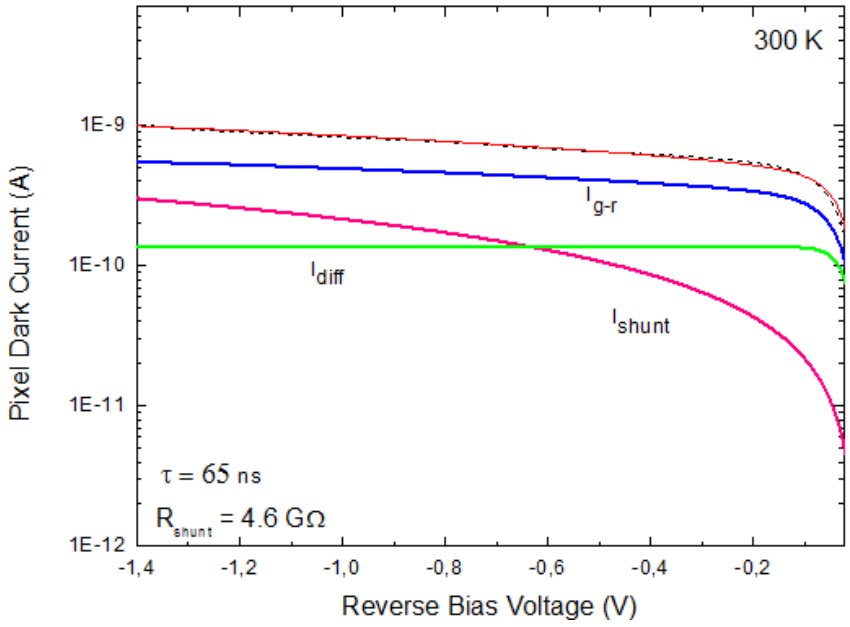

Figure 3.17: The dark current modelling of a test pixel with 15x15 μm^2 pixel area at 300 K.

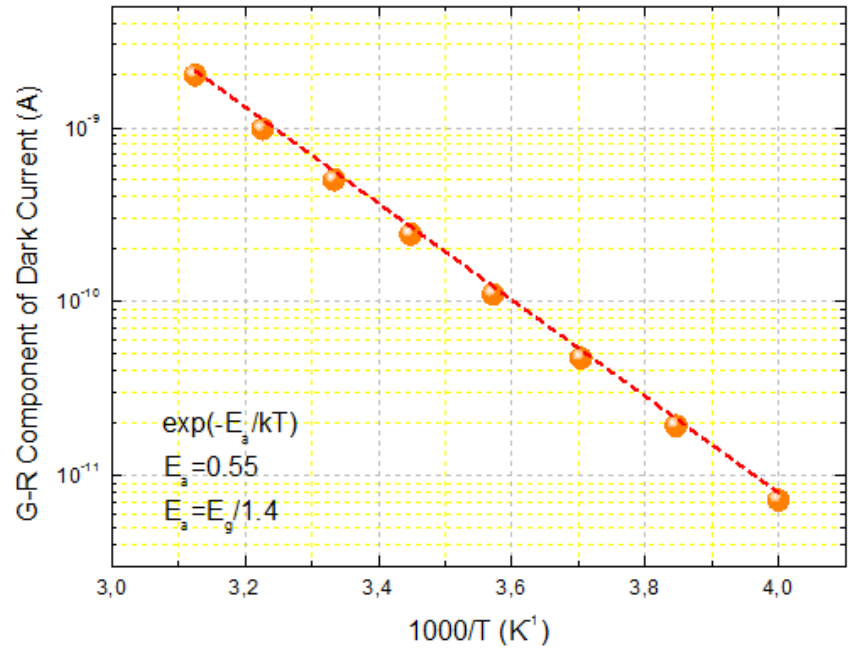

Figure 3.18: The G-R component of dark current versus temperature for test pixel with 15x15 μm^2 pixel area under 100 mV reverse bias voltage.

Figure 3.19 illustrates the variation of shunt resistance with respect to temperature. The activation energy being $E_g/2$ suggest that ohmic leakage current of test pixels has more effect on dark current when compared with test detectors having the activation energy of $E_g/1.8$. As the pixel pitch decreases, dark current of the detectors degrades due to surface related dark current which results from non-perfect passivation of the sidewalls. Therefore, the G-R lifetime of test pixels is smaller than that of the larger area test detectors.

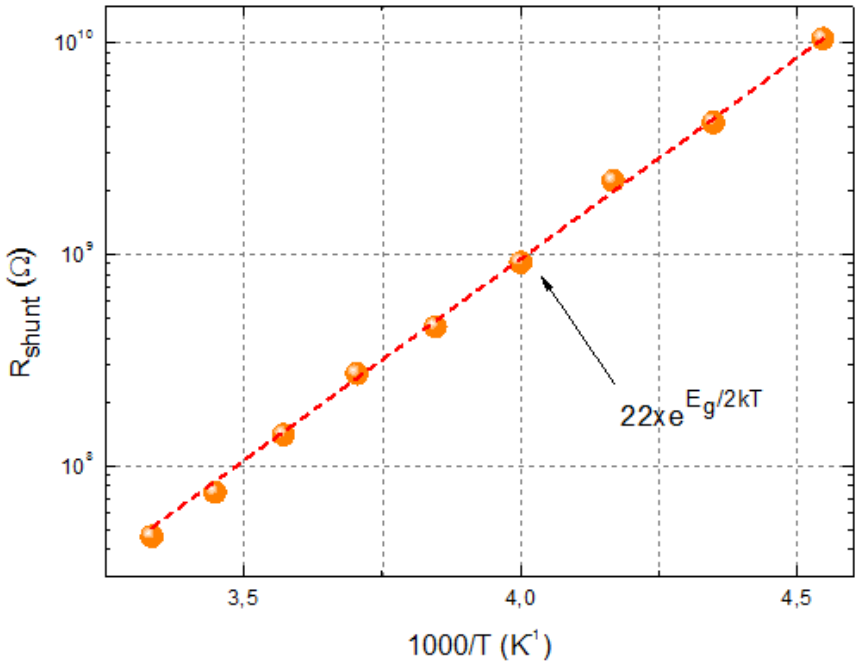

Figure 3.19: The variation of shunt resistance with temperature.

Figure 3.20 shows the corresponding single pixel I-V curves which are taken from different pixel groups including either 25 or 100 pixels connected in shunt for more reliable electrical characterization. In order to make the assessment easy, each pixel group is scaled down to a single pixel.

Figure 3.21 illustrates the I-V characteristic of a test pixel under dark conditions at various temperature levels. The dark current density of the test pixels is measured as 96 $\mu A/cm^2$ at 290 K under 0.1 V reverse bias. The variation of the dynamic resistance of the FPA pixels with reverse bias voltage is shown in Figure 3.22.

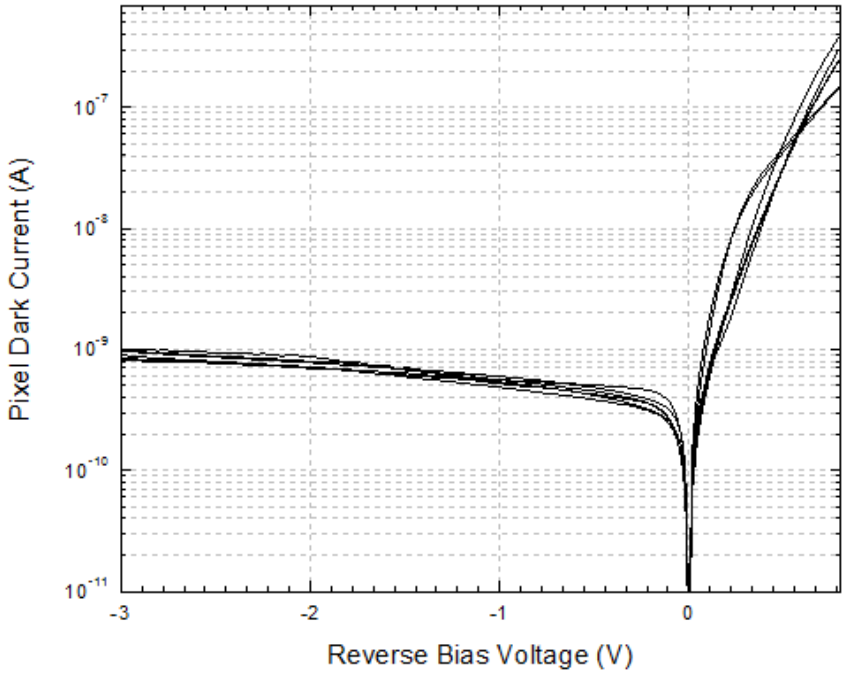

Figure 3.20: I-V characteristics of different pixel groups scaled to one pixel.

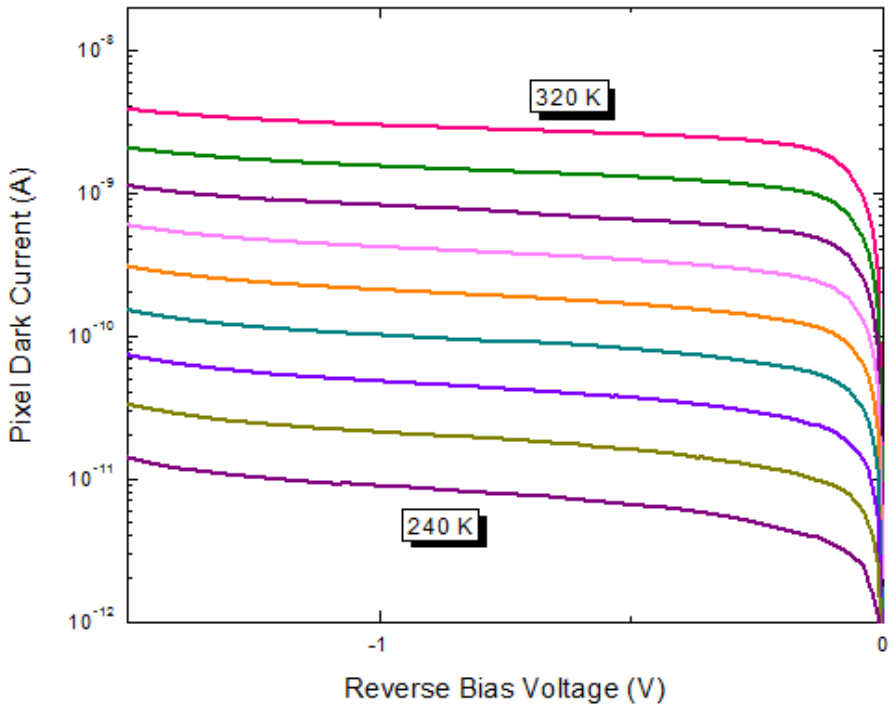

Figure 3.21: The I-V characterization of a test pixel at various temperatures.

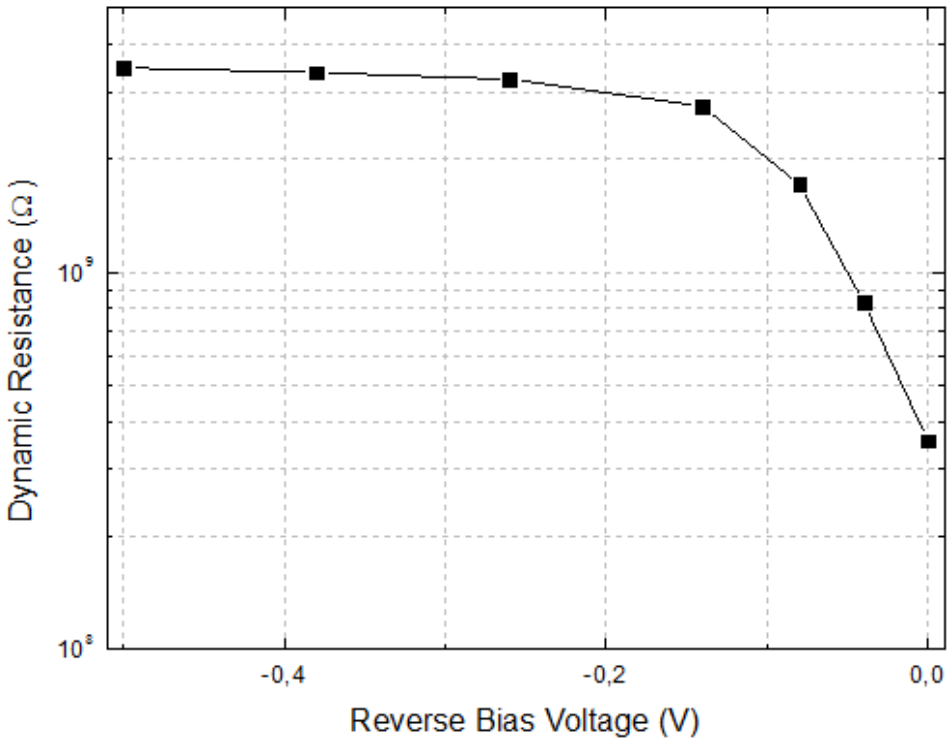

Figure 3.22: The plot of dynamic resistance versus reverse bias voltage.

3.3.4. Optical Characterization of Test Pixels

The most important performance parameters for a photodetector are responsivity, noise and detectivity. The responsivity measurement of the test pixels was conducted with Newport optical measurement system at room temperature under a reverse bias of 100 mV. The peak responsivity of the test detector was found to be 0.8 A/W. The Johnson noise limited detectivity of the pixels was ~1x10^{12}cm$\sqrt{Hz}$ /W at room temperature.

CHAPTER 4

CONCLUSION AND FUTURE WORK

In this thesis work, the pixels of a large format (640x512) $In_{0.53}Ga_{0.47}As$ FPA with 15 μm pixel pitch were characterized together with larger area test detectors. The mesa type pixel arrangement was utilized as the detector structure and uniform mesa sidewalls were obtained after several etch tests with different chemicals. In order to suppress the surface leakage current, a suitable passivation material was also applied. The detector array was hybridized to MT6415CA ROIC which was designed by Mikro Tasarım Ltd. for SWIR InGaAs detectors.

A detailed dark current analysis was conducted to provide feedback for the following works. With the purpose of specifying dominant dark current component, a model including diffusion, G-R and shunt currents was utilized. Firstly, this model was fitted to experimental results of test detectors with the area of 125x125 μm^2. The fitting results indicate that test detectors display bulk G-R dominated dark current behavior at 300 K. The G-R lifetime of test detector is 1.5 μs at 300 K. The most of the dark current of test detectors with the area equal to and larger than 75x75 μm^2 is bulk generated. The trap responsible for the G-R component of the dark current was further investigated through modeling and DLTS measurements. The fitting result shows a trap located at the energy level of 0.17 eV with respect to the E_i. The DLTS measurements yielded a minority trap with activation energy, density and the cross-section area of 0.52 eV, $9.87x10^{14}$ cm^3 and $8.78x10^{-15}$ cm^{-3}, respectively. The energy level of the trap detected by DLTS measurements was close to the trap level extracted from G-R lifetime plot suggesting that this trap is responsible for the G-R current dominating the dark current of the large area test detectors.

Test pixels identical to FPA pixel were also characterized with the purpose of determining the dominant dark current in FPA sized pixels. The G-R lifetime of test pixels was found to be 65 ns. As the pixel pitch decreases, dark current of the detector degrades due to surface related dark current resulting from non-perfect passivation of the sidewalls. Therefore, as a future work, passivation of the detectors can be studied through a more extensive work in order to improve the performance of the FPA pixels. Growth studies under different conditions may also be conducted in order to suppress the G-R component of the dark current by decreasing the trap density responsible for this current.

REFERENCES

[1] A. Rogalski, “Optical Detectors for Focal Plane Arrays,” Opto-Electronics Rev., vol. 12, no. 2, pp. 221–245, 2004.

[2] A. Daniels, “Field Guide to Infrared Systems, Detectors, and FPAs,” Second ed. Bellingham, Wash: SPIE Press, 2010.

[3] G. Gaussorgues, “Infrared Thermography,” First ed. London: Chapman & Hall, 1994.

[4] A. Rogalski, “Infrared Detectors,” Second ed. New York: CRC Press, 2011.

[5] C.Beşikci, “Infrared Devices and Systems Lecture Notes,” Ankara: METU, 2015.

[6] J. D. Vincent, S. E. Hodges, J. Vampola, M. Stegall, and G. Pierce, “Fundamentals of Infrared and Visible Detector Operation and Testing,” Second ed. New Jersey: Wiley, 2016.

[7] A. Rogalski and K. Chrzanowski, “Infrared Devices and Techniques,” Opto-Electronics Rev., vol. 10, no. 2, pp. 111–136, 2002.

[8] A. Rogalski, “Progress in Focal Plane Array Technologies,” Prog. Quantum Electron., vol. 36, no. 2, pp. 342–473, 2012.

[9] A. Rogalski, “Quantum Well Photoconductors in Infrared Detector Technology,” J. Appl. Phys., vol. 93, no. 8, pp. 4355–4391, 2003.

[10] S. Özer, “InSb and InAsSb Infrared Photodiodes on Alternative Substrates and InP/InGaAs Quantum Well Infrared Photodetectors: Pixel and Focal Plane Array Performance,” PhD Thesis. Turkey, 2005.

[11] Z. Jakšić, “Micro and Nanophotonics for Semiconductor Infrared Detectors: Towards an Ultimate Uncooled Device,” First ed. Switzerland: Springer, 2014.

[12] R. G. Driggers, V. Hodgkin, and R. Vollmerhausen, “What Good is SWIR? Passive Day Comparison of VIS, NIR, and SWIR,” Proc. SPIE - Infrared Imaging Syst. Des. Anal. Model. Test. XXIV, vol. 8706, p. 87060L, 2013.

[13] P. Chorier, P. Tribolet, P. Fillon, and A. Manissadjian, “Application Needs and Trade-offs for Short Wave Infrared Detectors,” Proc. SPIE - Infrared Imaging Syst. Des. Anal. Model. Test. XXIV Infrared Technol. Appl. XXIX, vol. 5074, pp. 363–373, 2003.

[14] M. P. Hansen and D. S. Malchow, “Overview of SWIR Detectors, Cameras, and Applications,” Proc. SPIE - Thermosense XXX, vol. 6939, p. 69390I, 2008.

[15] “SWIR Imaging: An Industrial Processing Tool.” [Online]. Available: https://www.photonics.com/EDU/Handbook.aspx. [Accessed: 02-Feb-2017].

[16] R. B. Smith, “Introduction to Hyperspectral Imaging,” First ed. MicroImages Inc., 2006.

[17] M. Macdougal, A. Hood, J. Geske, J. Wang, F. Patel, D. Follman, J. Manzo, and J. Getty, “InGaAs Focal Plan Arrays for Low-light-level SWIR Imaging,” Proc. SPIE - Infrared Technol. Appl. XXXVII, vol. 8012, p. 83530A, 2012.

[18] Y. Reibel, A. Rouvie, A. Nedelcu, T. Augey, N. Pere-Laperne, L. Rubaldo, D. Billon-Lanfrey, O. Gravrand, J. Rothman, and G. Destefanis, “Large Format, Small Pixel Pitch and Hot Detectors at SOFRADIR,” Proc. SPIE - Electro-Optical Infrared Syst. Technol. Appl. X, vol. 8896, p. 88960B, 2013.

[19] A. Rouvié, J. Coussement, O. Huet, J. P. Truffer, M. Pozzi, E. H. Oubensaid, S. Hamard, P. Maillart, and E. Costard, “InGaAs Focal Plane Array Developments and Perspectives,” Proc. SPIE - Infrared Technol. Appl. XLI, vol. 9451, p. 945105, 2014.

[20] M. MacDougal, A. Hood, J. Geske, C. Wang, D. Renner, D. Follman, and P. Heu, “Wide-area SWIR Arrays and Active Illuminators,” Proc. SPIE -

Quantum Sens. Nanophotonics Devices IX, vol. 8268, p. 82682Y, 2012.

[21] J. Allen, D. C. Dayton, J. D. Gonglewski, M. M. Myers, and R. Nolasco, "Seasonal Hemispherical SWIR Airglow Imaging," Proc. SPIE - Unconv. Imaging, Wavefront Sensing, Adapt. Coded Aperture Imaging Non-Imaging Sens. Syst., vol. 8165, p. 81650P, 2011.

[22] S. Derelle, P. Simoneau, J. Deschamps, S. Rommeluère, M. Hersé, G. Moreels, E. De Borniol, and O. Pacaud, "Development of Low Flux SWIR Radio-imaging Systems to Study Nightglow Emission," Proc. SPIE - Infrared Technol. Appl. XXXVIII, vol. 8353, p. 83533P, 2012.

[23] F. Guellec, S. Dubois, E. de Borniol, P. Castelein, S. Martin, R. Guiguet, M. Tchagaspanian, A. Rouvié, and P. Bois, "A Low-noise, 15µm Pixel-pitch, 640x512 Hybrid InGaAs Image Sensor for Night Vision," Proc. SPIE - Sensors, Cameras, Syst. Ind. Sci. Appl. XIII, vol. 8298, p. 82980C, 2012.

[24] W. Vereecken, U. Van Bogget, T. Colin, R.-M. Vinelli, J. Das, P. Merken, and J. Vermeiren, "A Low Noise, Extended Dynamic Range 1.3 Megapixel InGaAs Array," Proc. SPIE - Infrared Technol. Appl. XXXIX, vol. 8704, p. 870404, 2013.

[25] J. Liu, R. Camacho-Aguilera, J. T. Bessette, X. Sun, X. Wang, Y. Cai, L. C. Kimerling, and J. Michel, "Ge-on-Si Optoelectronics," Thin Solid Films, vol. 520, no. 8, pp. 3354–3360, 2012.

[26] Z. Huang, J. Oh, and J. C. Campbell, "Back-side-illuminated High-speed Ge Photodetector Fabricated on Si Substrate Using Thin SiGe Buffer Layers," Appl. Phys. Lett., vol. 85, no. 15, pp. 3286–3288, 2004.

[27] L. Chen, X. Huang, M. Li, Y. Huang, Y. Wang, G. Yan, and C. Li, "High-performance Ge p-i-n Photodetector on Si Substrate," Optoelectron. Lett., vol. 11, no. 3, pp. 195–198, 2015.

[28] L. Colace, G. Masini, G. Assanto, H.-C. Luan, K. Wada, and L. C. Kimerling,

"Efficient High-speed Near-infrared Ge Photodetectors Integrated on Si Substrates," Appl. Phys. Lett., vol. 76, no. 10, pp. 1231–1233, 2000.

[29] I. Aberg, B. Ackland, J. V Beach, C. Godek, R. Johnson, C. A. King, A. Lattes, J. O. Neill, S. Pappas, T. S. Sriram, C. S. Rafferty, N. V. Corporation, and E. Drive, "A Low Dark Current and High Quantum Efficiency Monolithic Germanium-on- Silicon CMOS Imager Technology for Day and Night Imaging Applications," IEE Proc. - Int. Electron Devices Meet. IEDM, vol. 978, no. 1, pp. 344–347, 2010.

[30] H. Figgemeier, M. Benecke, K. Hofmann, R. Oelmaier, A. Sieck, J. Wendler, and J. Ziegler, "SWIR Detectors for Night Vision at AIM," Proc. SPIE - Infrared Technol. Appl. XL, vol. 9070, p. 907008, 2014.

[31] P. Chorier and P. Tribolet, "High Performance HgCdTe SWIR Detectors Development at Sofradir," Proc. SPIE - Infrared Technol. Appl. XXVII, vol. 4369, pp. 698–712, 2001.

[32] J. Piotrowski and A. Rogalski, "High-Operating-Temperature Infrared Photodetectors," First ed. Bellingham, Wash: SPIE Press, 2007.

[33] M. Henini and M. Razeghi, "Handbook of Infrared Detection Technologies," First ed. New York: Elsevier, 2002.

[34] J. Antoszewski, N. M. Akhavan, G. Umana-Membreno, R. Gu, W. Lei, and L. Faraone, "Recent Developments in Mercury Cadmium Telluride IR Detector Technology," ECS Trans., vol. 69, no. 14, pp. 61–75, 2015.

[35] A. Weber, M. Benecke, J. Wendler, A. Sieck, D. Hübner, H. Figgemeier, and R. Breiter, "Extended SWIR Imaging Sensors for Hyperspectral Imaging Applications," Proc. SPIE - Image Sens. Technol. Mater. Devices, Syst. Appl. III, vol. 9854, p. 98540C, 2016.

[36] S. Paul, J. B. Roy, and P. K. Basu, "Empirical Expressions for the Alloy Composition and Temperature Dependence of the Band Gap and Intrinsic

Carrier Density in $Ga_xIn_{1-x}As$," J. Appl. Phys., vol. 69, no. 2, pp. 827–829, 1991.

[37] M. Levinshtein, S. Rumyantsev, and M. Shur, "Handbook Series on Semiconductor Parameters , Ternary and Quaternary III-V Compounds," London: World Scientific Publishing, 1999.

[38] Y. Zhang and Y. Gu, "Gas Source MBE Grown Wavelength Extending InGaAs Photodetectors," in Advances in Photodiodes, InTech, 2011, pp. 349–376.

[39] Y. Zhang, Y. Gu, Z. Tian, A. Li, X. Zhu, and K. Wang, "Wavelength Extended InGaAs/InAlAs/InP Photodetectors Using n-on-p Configuration Optimized for Back Illumination," Infrared Phys. Technol., vol. 52, no. 1, pp. 52–56, 2009.

[40] C. Li, Y. Zhang, K. Wang, Y. Gu, H. Li, and Y. Li, "Distinction Investigation of InGaAs Photodetectors Cutoff at 2.9 μm," Infrared Phys. Technol., vol. 53, no. 3, pp. 173–176, 2010.

[41] Y. Arslan, F. Oguz, and C. Besikci, "640 × 512 Extended Short Wavelength Infrared $In_{0.83}Ga_{0.17}As$ Focal Plane Array," IEEE J. Quantum Electron., vol. 50, no. 12, pp. 957–964, 2014.

[42] A. I. Graded, L. Wavelengths, K. R. Linga, G. H. Olsen, V. S. Ban, A. M. Joshi, and W. F. Kosonocky, "Dark Current Analysis and Characterization of $In_xGa_{1-x}As/InAs_yP_{1-y}$ Graded Photodiodes with x>0.53 for Response to Longer Wavelengths (>1.7μm)," J. Light. Technol., vol. 10, no. 8, pp. 1050–1055, 1992.

[43] T. Martin, R. Brubaker, P. Dixon, M. Gagliardi, and T. Sudol, "640x512 InGaAs Focal Plane Array Camera for Visible and SWIR Imaging," Proc. SPIE - Infrared Technol. Appl. XXXI, vol. 5783, pp. 12–20, 2005.

[44] B. M. Onat, W. Huang, N. Masaun, M. Lange, M. H. Ettenberg, and C. Dries,

"Ultra Low Dark Current InGaAs Technology for Focal Plane Arrays for Low-light Level Visible-shortwave Infrared Imaging," Proc. SPIE - Infrared Technol. Appl. XXXIII, vol. 6542, p. 65420L, 2007.

[45] P. Dixon, N. Masaun, M. Evans, J. U. McHale, J. Trezza, and M. Ettenberg, "Monolithic Planar InGaAs Detector Arrays for Uncooled High-sensitivity SWIR Imaging," Proc. SPIE - Airborne Intell. Surveillance, Reconnaiss. Syst. Appl. VI, vol. 7307, p. 730706, 2009.

[46] B. E. A. Saleh and M. C. Teich, "Fundamentals of Photonics," Second ed. New Jersey: Wiley, 2007.

[47] H. Tang, X. Wu, K. Zhang, L. Ye, N. Wang, X. Li, and H. Gong, "High Uniformity InGaAs Linear Mesa-type SWIR Focal Plane Arrays," Infrared Mater. Devices Appl., vol. 6835, no. 1, p. 683516, 2007.

[48] Y. Rsuji, Y. Tsuji, K. Hiratsuka, and H. Yano, "Fabrication of Mesa-type InGaAs pin PDs with InP Passivation Structure on 4-inch Diameter InP Substrate," IEEE Proc. - Intemational Conf. Indium Phoshide Relat. Mater., pp. 245–248, 2004.

[49] C. P. Skrimshire, J. R. Farr, D. F. Sloan, M. J. Robertson, P. A. Putland, J. C. D. Stokoe, and R. R. Sutherland, "Reliability of Mesa and Planar InGaAs PIN Photodiodes," Optoelectronics, vol. 137, no. 1, pp. 74–78, 1990.

[50] A. Rouvié, J.-L. Reverchon, O. Huet, A. Djedidi, J.-A. Robo, J.-P. Truffer, T. Bria, M. Pires, J. Decobert, and E. Costard, "InGaAs Focal Plane Array Developments at III-V Lab," Proc. SPIE - Infrared Technol. Appl. XXXVIII, vol. 8353, p. 835308, 2012.

[51] A. Rouvié, O. Huet, S. Hamard, J. P. Truffer, M. Pozzi, J. Decobert, E. Costard, M. Zécri, P. Maillart, Y. Reibel, and A. Pécheur, "SWIR InGaAs Focal Plane Arrays in France," Proc. SPIE - Infrared Technol. Appl. XXXIX, vol. 8704, p. 870403, 2013.

[52] A. Rouvié, O. Huet, J. L. Reverchon, J. A. Robo, J. P. Truffer, J. Decobert, E. Costard, and P. Bois, “15 μm Pixel-pitch VGA InGaAs Module for Very Low Background Applications,” Proc. SPIE - Sensors, Syst. Next-Generation Satell. XV, vol. 8176, p. 81761A, 2011.

[53] J. Coussement, A. Rouvié, E. H. Oubensaid, O. Huet, S. Hamard, J.-P. Truffer, M. Pozzi, P. Maillart, Y. Reibel, E. Costard, and D. Billon-Lanfrey, “New Developments on InGaAs Focal Plane Array,” Proc. SPIE - Infrared Technol. Appl. XL, vol. 9070, p. 907005, 2014.

[54] F. Rutz, P. Kleinow, R. Aidam, W. Bronner, L. Kirste, and M. Walther, “InGaAs Infrared Detector Development for SWIR Imaging Applications,” SPIE Proceeding - Electro-Optical Infrared Syst. Technol. Appl. X, vol. 8896, p. 88960C, 2013.

[55] P. Kleinow, F. Rutz, R. Aidam, W. Bronner, H. Heussen, and M. Walther, “Optimization of InGaAs/InAlAs APDs for SWIR Detection with Demand for High Gain and Low Breakdown Voltage,” SPIE Proceeding - Electro-Optical Infrared Syst. Technol. Appl. XI, vol. 9249, p. 92490X, 2014.

[56] F. Rutz, P. Kleinow, M. Walther, R. Aidam, W. Bronner, L. Kirste, J. Niemasz, R. Rehm, J. Schmitz, T. Stadelmann, M. Wauro, A. Wörl, A. Sieck, and J. Ziegler, “Infrared Photodetector Development at Fraunhofer IAF,” SPIE Proceeding - Quantum Sens. Nanophotonic Devices XI, vol. 8993, p. 89930W, 2013.

[57] F. Rutz, P. Kleinow, R. Aidam, H. Heussen, W. Bronner, A. Sieck, and M. Walther, “SWIR Photodetector Development at Fraunhofer IAF,” Proc. SPIE - Image Sens. Technol. Mater. Devices, Syst. Appl. II, vol. 9481, p. 948107, 2015.

[58] F. Rutz, P. Kleinow, R. Aidam, W. Bronner, L. Stolch, M. Benecke, A. Sieck, and R. Rehm, “SWIR Detectors for Low Photon Fluxes,” Proc. SPIE - Infrared Sensors, Devices, Appl. VI, vol. 9974, p. 99740G, 2016.

[59] S. Eminoglu, M. Isikhan, N. Bayhan, M. A. Gulden, O. S. Incedere, S. T. Soyer, S. Kocak, S. Y. Gokhan, and T. Akin, "MT6415CA A 640×512-15μm CTIA ROIC for SWIR InGaAs Detector Arrays," Proc. SPIE - Int. Soc. Opt. Eng., vol. 8704, pp. 1–9, 2013.

[60] J. Nguyen, D. Z. Ting, C. J. Hill, A. Soibel, S. A. Keo, and S. D. Gunapala, "Dark Current Analysis of InAs / GaSb Superlattices at Low Temperatures," Infrared Phys. Technol., vol. 52, no. 6, pp. 317–321, 2009.

[61] S. R. Forrest, "Performance of $ln_xGa_{1-x}As_yP_{1-y}$, Photodiodes with Dark Current Limited by Diffusion , Generation Recombination , and TunneIing," IEEE J. Quantum Electron., vol. QE-17, no. 2, pp. 217–226, 1981.

[62] S. R. Forrest, R. F. Leheny, R. E. Nahory, and M. A. Pollack, "$In_{0.53}Ga_{0.47}As$ Photodiodes With Dark Current Limited by Generation Recombination and Tunneling," Appl. Phys. Lett., vol. 37, pp. 322–324, 1980.

[63] X. D. Wang, W. D. Hu, X. S. Chen, W. Lu, H. J. Tang, T. Li, and H. M. Gong, "Dark Current Simulation of InP/$In_{0.53}Ga_{0.47}As$/InP p-i-n Photodiode," Opt Quant Electron, vol. 40, pp. 1261–1266, 2008.

[64] D. V Lang, "Deep-level Transient Spectroscopy : A New Method to Characterize Traps in Semiconductors," J. Appl. Phys., vol. 45, no. 7, pp. 3023–3032, 1974.

[65] R. K. Ahrenkiel, R. Ellingson, S. Johnston, and M. Wanlass, "Recombination Lifetime of $In_{0.53}Ga_{0.47}As$ as a Function of Doping Density," Appl. Phys. Lett., vol. 72, no. 26, pp. 3470–3472, 1998.